



Chair of
Solar Technology

RWTHAACHEN
UNIVERSITY

The present work was submitted to Chair of Solar Technology (DLR)

Diese Arbeit wurde vorgelegt am Lehrstuhl für Solartechnik (DLR)

**Implementation of a particle-heated bayonet reactor for solar production of hydrogen
in the HyS process and techno-economic analysis**

Implementierung eines partikelbeheizten Bajonett-Reaktors für die solare Produktion von
Wasserstoff im HyS-Prozess und techno-ökonomische Analyse

Master thesis

Masterarbeit

von / presented by

Pascal Kircher

356588

Prof. Dr.-Ing. Robert Pitz-Paal

Dr.-Ing. Bernhard Hoffschmidt

Gkiokchan Moumin

Aachen, September 29, 2021

Abstract

The growing demand for hydrogen increases the call for processes that can produce hydrogen on large scales. The Hybrid Sulfur cycle powered with concentrated solar power is a potential candidate as it can deliver energy-efficiently produced green hydrogen on large scales. To produce hydrogen, sulfurous acid is processed using electrochemical procedures. The hereby formed sulfuric acid will be cracked with thermal energy, which are provided by bauxite particles heated through concentrated solar power. To recover heat from the sulfuric acid cracking, a Bayonet reactor developed at Sandia National Laboratory is used.

This thesis observes different production scales of the Hybrid Sulfur cycle to satisfy the fuel or oxygen demand of the copper production in Olympic Dam (Australia). The fuel demand aroused from the furnaces of the copper production is satisfied by the produced hydrogen. This thesis uses different simulation tools to depict the different parts of the solar-powered Hybrid Sulfur cycle.

A detailed model of the Bayonet reactor was created through the cooperation of Python and Aspen Plus. The reactor operates at 15 bar and therefore requires a minimum temperature of 925 °C in the catalytic section to stabilize the used iron oxide catalyst. A theoretical Bayonet model with a minimum catalytic temperature of 800 °C is introduced to observe the benefits resulting from that assumption. Both Bayonet models are implemented in a Hybrid Sulfur cycle flowsheet in Aspen Plus. To simulate the concentrated solar thermal energy system Python is used. Beforehand, a heliostat field was designed using heliostat field layout calculation software from the German Aerospace Center DLR. To evaluate the complete process, techno-economic analyses were performed.

The lowest levelized costs of hydrogen ($4.42 \frac{\text{€}}{\text{kg}}$) are yielded by the largest observed scale, where the Hybrid Sulfur cycle is required to produce $81 \frac{\text{t}_{\text{H}_2}}{\text{d}}$. A sensitivity analysis for different assumptions showed potentials to lower these costs down to $3.27 \frac{\text{€}}{\text{kg}}$. The price range for conventionally produced hydrogen from fossil fuels of $0.93\text{-}1.55 \frac{\text{€}}{\text{kg}}$ is not reached, but clear benefits in comparison to alkaline electrolytic procedures are shown.

Assignment

Die nachhaltige Herstellung von Wasserstoff ist eine der zentralen Fragestellungen unserer Zeit. Ein vielversprechender Prozess ist die depolarisierte Elektrolyse (SDE), in der Wasser zusammen mit Schwefeldioxid zu Wasserstoff und Schwefelsäure umgesetzt wird. Der Vorteil: Die SDE weist dabei nur einen Drittel des Strombedarfs der reinen Wasserelektrolyse auf. Um die Schwefelsäure erneut dem Elektrolyseur zuführen zu können, muss diese bei 800-1000 °C in ihre Bestandteile Schwefeldioxid, Wasser und Sauerstoff gespalten werden. Dieses Temperaturniveau kann über konzentrierte Solarenergie bereitgestellt werden, wodurch die Wasserstoffproduktion nachhaltig und auch kostentechnisch attraktiv wird. Eine der effizientesten Technologien für die solare Wärmebereitstellung ist die Nutzung eines Partikelreceivers, in dem die Strahlung durch Partikel absorbiert wird, die wiederum dem Spaltungsreaktor zugeführt werden.

Die Aufgabe im Rahmen der Masterarbeit ist die Erweiterung eines bestehenden Schwefelsäure Kreisprozesses zur Einbindung eines Partikelreceivers. Dabei sind die neuen Randbedingungen bezüglich der Receiverperformance und Wärmeübertragung an den Bajonett-Spaltungsreaktor zu implementieren. Kritische technische Limitierungen sind aufzuzeigen und Lösungen hierfür sind zu erarbeiten. Das Gesamtsystem soll hinsichtlich der Kosten optimiert werden, wobei lokale Einstrahlungsgegebenheiten genauso eine Rolle spielen wie die Nutzung der Produktströme Wasserstoff und Sauerstoff. Die Kopplung des Prozesses an den Industrieprozess der Kupferproduktion an einem sonnenreichen Standort wie Australien ist beispielhaft durchzuführen.

Eidesstattliche Erklärung

Name, Vorname

Matrikelnummer (freiwillige Angabe)

Ich versichere hiermit an Eides Statt, dass ich die vorliegende Projektarbeit/Bachelorarbeit/Masterarbeit* mit dem Titel

selbständig und ohne unzulässige fremde Hilfe erbracht habe. Ich habe keine anderen als die angegebenen Quellen und Hilfsmittel benutzt. Für den Fall, dass die Arbeit zusätzlich auf einem Datenträger eingereicht wird, erkläre ich, dass die schriftliche und die elektronische Form vollständig übereinstimmen. Die Arbeit hat in gleicher oder ähnlicher Form noch keiner Prüfungsbehörde vorgelegen. Ich erkläre mich hiermit einverstanden, dass die vorliegende Arbeit in der Lehrstuhlbibliothek aufbewahrt wird und kopiert werden darf und habe keine Einwände gegen eine Veröffentlichung der gesamten Arbeit oder von einzelnen Teilen daraus.

Ort, Datum

Unterschrift

*Nichtzutreffendes bitte streichen

Belehrung:

§156 StGB: Falsche Versicherung an Eides Statt

Wer vor einer zur Abnahme einer Versicherung an Eides Statt zuständigen Behörde eine solche Versicherung falsch abgibt oder unter Berufung auf eine solche Versicherung falsch aussagt, wird mit Freiheitsstrafe bis zu drei Jahren oder mit Geldstrafe bestraft.

§161 StGB: Fahrlässiger Falscheid; fahrlässige falsche Versicherung an Eides Statt

(1) Wenn eine der in den §§154 bis 156 bezeichneten Handlungen aus Fahrlässigkeit begangen worden ist, so tritt Freiheitsstrafe bis zu einem Jahr oder Geldstrafe ein.

(2) Straflosigkeit tritt ein, wenn der Täter die falsche Angabe rechtzeitig berichtigt. Die Vorschriften des § 158 Abs. 2 und 3 gelten entsprechend.

Die vorstehende Belehrung habe ich zur Kenntnis genommen:

Ort, Datum

Unterschrift

Erklärung

Ich erkläre mich hiermit einverstanden, dass die vorliegende Arbeit in der Lehrstuhlbibliothek aufbewahrt wird und kopiert werden darf und habe keine Einwände gegen eine Veröffentlichung der gesamten Arbeit oder von einzelnen Teilen daraus.

Ich bin damit einverstanden, dass die RWTH Aachen folgende Daten zu meiner Person im Internet veröffentlicht: Name, Vorname, Titel der Arbeit.

Mir ist bekannt,

- dass ich diese Einwilligung jederzeit schriftlich mit Wirkung für die Zukunft widerrufen kann und meine elektronisch gespeicherten Daten unverzüglich gelöscht werden müssen und
- die Aachener Verfahrenstechnik bei Widerruf meiner Einwilligung verpflichtet ist, mein Werk aus der Bibliothek des Instituts/Lehrstuhls zu entfernen.

Ort, Datum

Unterschrift

Contents

1	Introduction	1
2	Background and State of the Art	2
2.1	The Hybrid Sulfur process	2
2.2	Bayonet reactor	5
2.3	Heat transfer modulation	7
2.4	Reaction kinetics	13
2.5	Concentrated solar power system	14
2.6	Economic analysis	16
3	Modelling	20
3.1	Bayonet reactor model	20
3.2	Scale-up and flowsheet integration	33
3.3	Solar system dimensioning	37
4	Results and Discussion	46
4.1	Bayonet Configurations	46
4.2	Techno-economic analysis	54
5	Conclusion and Outlook	63
	List of Abbreviations	66
	Bibliography	72
	List of Figures	81
A	Appendix	83

1 Introduction

Currently, over 80 % of the worldwide energy demand is satisfied by burning fossil fuels [1]. The Intergovernmental Panel on Climate Change (IPCC) clearly stated that climate change and the coherent consequences that currently can be observed are related to the anthropogenic emission of carbon dioxide [2]. Therefore, a drastic transition to more climate-friendly energy supply methods is needed. Hydrogen is a promising fuel alternative because it has a high energy content and does not emit carbon dioxide while burning. Additionally, hydrogen is often required as a reactant for synthesizing specialty chemicals and is therefore very versatile.

Another high polluting sector is the transport sector. As hydrogen can be used in fuel cells as well as in combustion engines or turbines, it is a good alternative to make this sector more climate-friendly. The DLR has a large effort to enable hydrogen fuel cell technology for aviation or shipping [3]. It can be seen, that the demand for hydrogen will increase and therefore methods to produce hydrogen on large scales become more important. The conventional production of hydrogen from fossil fuels, like the natural gas steam reforming, also emits carbon dioxide and is therefore not sustainable. Green alternatives are the electrolysis of water with renewable energy, biogas reforming or thermochemical water splitting. Electricity from the grid is currently not completely renewable. In Germany e.g. the fraction of renewable electricity in the grid was 45.4 % in 2020 as the German Environment Agency has stated [4]. Thus, using electrolytic procedures that require less electricity to produce hydrogen is favorable for grid-supplied productions. The Sulfur Dioxide Depolarised Electrolysis requires approximately one third of the energy, that standard alkaline electrolysis would require [5]. The Hybrid Sulfur cycle runs the Sulfur Dioxide Depolarised Electrolysis. The simulation and techno-economic evaluation of the Hybrid Sulfur cycle will be the content of the following chapter.

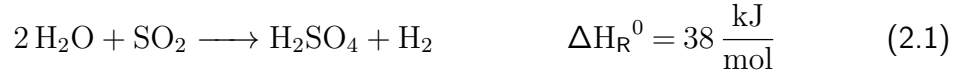
2 Background and State of the Art

This chapter covers the required theoretical background needed for this thesis. Starting with the main subject - the Hybrid Sulfur process (section 2.1). This process contains a decomposition of sulfuric acid, proceeded in a so-called Bayonet reactor (section 2.2). The explicit modulation of this reactor requires heat transfer models (section 2.3) and reaction kinetics for the sulfuric acid decomposition (section 2.4). The high demand for thermal energy during the HyS process is produced using a concentrated solar thermal energy system (section 2.5). Finally, the theoretical backgrounds to economic analysis (section 2.6) are discussed.

2.1 The Hybrid Sulfur process

As the production of high quantities of hydrogen is important for the current energy revolution, many different production methods were investigated during the last couple of decades. To produce hydrogen without emitting carbon dioxide (CO_2), so-called green hydrogen, only water can be used as source material. Besides alkaline electrolysis, heat-driven chemical reactions with recirculation of intermediate substances (thermochemical processes) can be used to split water into hydrogen and oxygen. Among the thermochemical processes, these using sulfur-based components are among the promising approaches [6]. The most important sulfur-based processes are the Hybrid Sulfur (HyS) process, the Sulfur Iodine (SI) process and the Sulfur Bromine cycle. In comparison to other sulfur-based processes, the HyS process uses a special electrolytic procedure for water splitting, the so-called Sulfur-Dioxide-Depolarised Electrolysis (SDE). The advantage of SDE is a significantly lower cell voltage of 0.158 V in contrast to 1.229 V for conventional electrolysis [7]. The cell voltage of the SDE is only theoretical and will not be reached by the electrolyzers as later explanations will show. The main advantage of the HyS process, despite the lower efficiency, is the comparatively simple

process design. The SI process, e.g. requires two extra reactors instead of the SDE and a complex separation step after the first of these reactors [8]. The electrochemical oxidation occurring during the SDE is shown in equation 2.1.



For the complete HyS-cycle, the formed sulfuric acid (H_2SO_4) needs to be dissociated (equation 2.2) and sulfur trioxide (SO_3) has to be reduced (equation 2.3). Both reactions are endothermic and form the process part of sulfuric acid cracking (SAC).



The temperature levels of the SAC step are between 400 and 1000 °C. While nuclear power plants were analyzed as CO_2 -free options to provide heat at these temperature levels [5], CSTE from solar towers can cover the need without the environmental disadvantage of nuclear power.

Figure 2.1 summarizes all important process parts for the HyS process. The decomposition of H_2SO_4 takes place in the Bayonet reactor which will be explained in detail in the next section (section 2.2). The thermal energy for the SAC section is provided by bauxite particles which are heated in a rotating particle receiver (CentRec). Further details on the solar integration will be given in section 2.5. After the SAC section, sulfur dioxide and oxygen are separated at lower temperatures. Sulfur dioxide is recirculated into the electrolyzer, while oxygen is extracted from the cycle for further use. The SDE then splits water as shown in reaction 2.1. Hydrogen is separated from the other products, purified and extracted from the plant. The remaining diluted H_2SO_4 is concentrated and recirculated to the SAC section.

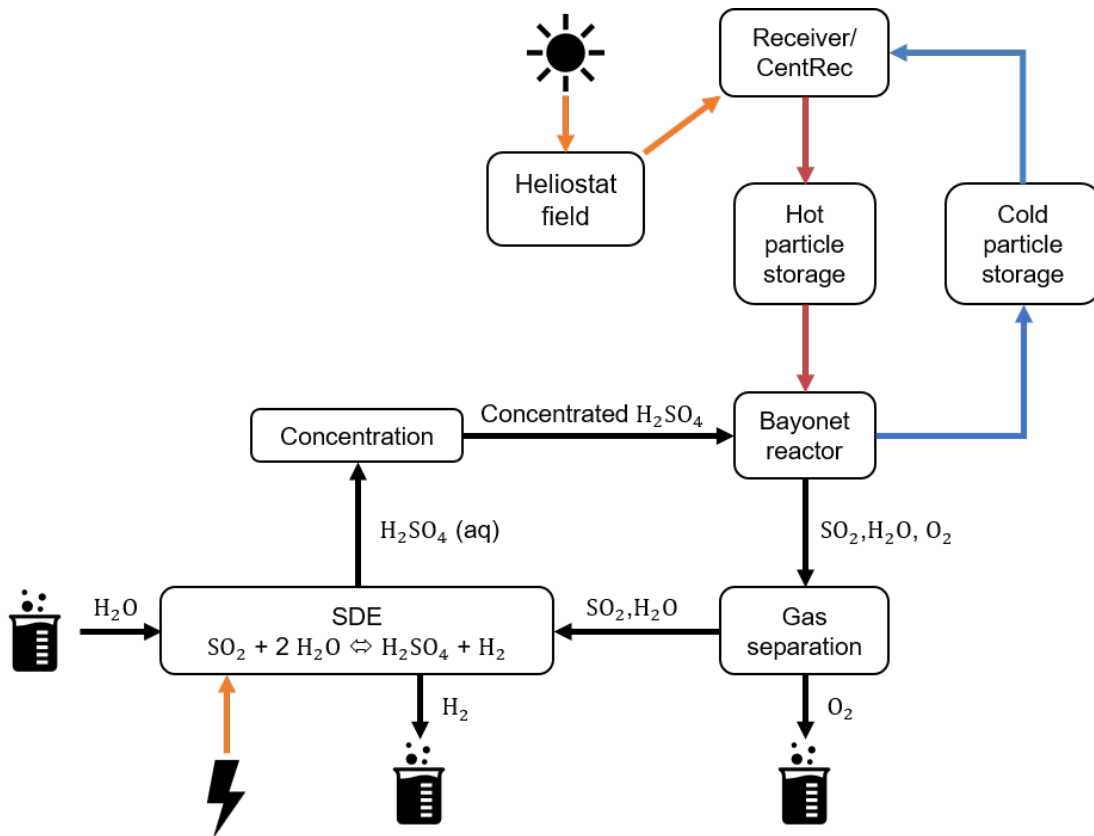


Figure 2.1: HyS process with CSTE plant using a particle heated bayonet reactor for acid splitting.

The concentration of the acid is required since an increased acid concentration can lower the heat demand of the SAC step as earlier studies noted [9],[10]. The electrolyzer for the SDE step has improved over the last decades as material development enhanced the stability and performance of the proton exchange membranes (PEM). State of the art is a sulfonated polybenzimidazole (s-PBI) membrane developed at the University of South Carolina (USC). It can achieve a cell voltage of 0.66 V and a current density of $0.5 \frac{\text{A}}{\text{cm}^2}$ [11]. As Gorenssek et al. [12] have shown, an output concentration of 65 wt.-% H₂SO₄ is possible using an s-PBI membrane, which requires $115.8 \frac{\text{kJ}}{\text{mol}_{\text{H}_2}}$ electric power.

Table 2.1 gives an overview of the existing HyS processes which are comparable to the set-up of this thesis. The used currency exchange rate is 1 EUR = 1.1767 USD as stated by the European Central Bank on 2021/08/17 [13]. The inflation was corrected using data for the consumer prices in Germany [14].

Table 2.1: Overview of HyS processes

Name	Year	Energy demand	LHV	LCoH	Source
		$[\frac{\text{kJ}}{\text{molH}_2}]$	efficiency [%]	$[\frac{\text{€}}{\text{kg}}]$	
Gorensek	2009	461.2	35.3	4.59-5.32	[9]
Corgnale	2011	473.7	33	2.79-4.20	[15]
Hinkley	2011	-	-	4.40	[16]
Tiax LLC	2011	450.7-562.5	32-39	3.37-4.97	[17]
del F. Acropinto	2021	581	30	5.73-6.72	[18]

2.2 Bayonet reactor

To close the HyS-cycle after the SDE section, the formed H_2SO_4 needs to be cracked into sulfur dioxide, oxygen and water. The first step is to vaporize H_2SO_4 . The gaseous sulfuric acid dissociates into water and SO_3 (equation 2.2). The subsequent decomposition of SO_3 (equation 2.3) is a very slow reaction, which does not reach equilibrium conversion under continuous reaction controls. Catalysts and high temperatures are required to enhance the occurring conversion rate. Section 2.4 will give a detailed overview of the possible catalysts and their behaviors.

To fulfill the high heat demand of these reactions using solar power, many different reactor designs were analyzed. The German Aerospace Center (DLR) has been developing a two sectional reactor concept with two directly irradiated absorbers in series, where the vaporization reaction and the catalytic decomposition reaction take place in separate units [19], [20]. The performance of directly irradiated reactor concepts depends on the current irradiation and is subject to daily and seasonal fluctuations [5]. Therefore, indirectly irradiated concepts seem to be easier to handle. One of these concepts is the "indirect heating concept of sulfuric acid decomposer/ SO_3 splitting reactor" presented by Agrafiotis et al. [21]. This concept consists of a bundle of tube reactors that are heated by a counter-current stream of bauxite particles on the shell side. The downside of this concept is a very hot reactor outlet, which could dam-

age subsequent process modules. The Bayonet reactor concept, invented as part of the U.S. Department of Energy (DOE) Nuclear Hydrogen Initiative [22] and demonstrated at Sandia National Laboratory (SNL) [23], can reuse the heat potential of the high reactor outlet by recycling the outlet stream through an inner tube as figure 2.2 shows.

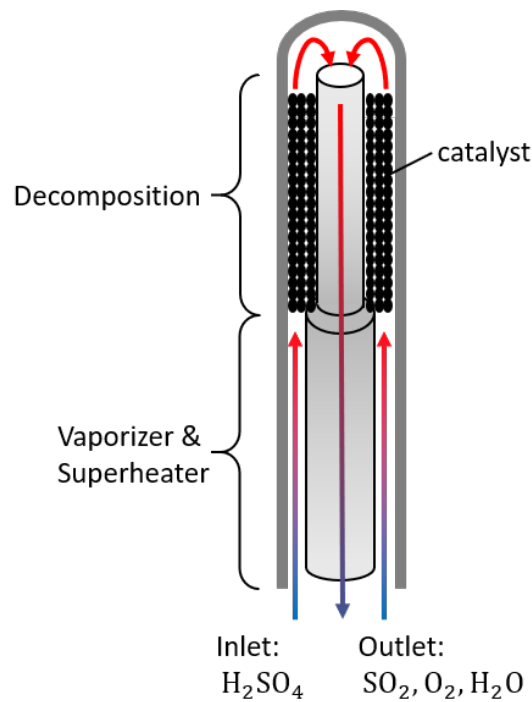


Figure 2.2: The Bayonet reactor for H_2SO_4 cracking [22],[23]

The arrows in figure 2.2 represent the flow direction of the reactor fluid. With blue coloring representing cold stream areas between 200 to 300 °C and red coloring representing hot stream areas. The highest temperature is reached at the reactor top before the gaseous stream is recycled through the inner tube. For the SNL test set-up, the reactor was heated using high-temperature air, streaming on the shell side of the Bayonet tube. This thesis will concentrate on the integration using solar-heated bauxite particles, as this heating method is a promising alternative due to its low cost and high temperature range. The particles will stream counter-current to the inlet stream direction on the shell side of the Bayonet tube. The maximum achievable temperature depends on the particle mass flow and the inlet temperature of the particle stream.

2.3 Heat transfer modulation

This section covers the heat transfer modulation according to the VDI heat atlas chapter G1 and G2 [24]. Starting with the general definition of heat transfer through a pipe wall (subsection 2.3). And ending with an overview of the different convection calculation models (subsection 2.3).

General heat transfer

The overall thermal transmittance U for the heat transfer through a simple pipe is defined by equation 2.4. The thermal transmittance summarizes the occurring thermal convection within the flowing fluids and the thermal conduction of the pipe wall.

$$U = \frac{1}{A \cdot \left[\frac{1}{\alpha_i \cdot A_i} + \frac{\ln(r_o/r_i)}{2 \cdot \pi \cdot \lambda \cdot L} + \frac{1}{\alpha_o \cdot A_o} \right]} \quad (2.4)$$

$$\dot{Q} = U \cdot A \cdot \frac{(T_{o,2} - T_{i,2}) - (T_{o,1} - T_{i,1})}{\ln\left(\frac{T_{o,2} - T_{i,2}}{T_{o,1} - T_{i,1}}\right)} \quad (2.5)$$

Equation 2.5 shows the yielding heat flow through a pipe segment for a given logarithmic temperature difference along the pipe. Figure 2.3 explains the different parameters of the equations above. With L representing the pipe length, A_o and A_i the outer and inner surface area respectively, r_o and r_i the outer and inner pipe radius, α_o and α_i the heat transfer coefficient for the outer and inner liquid stream, λ the thermal conductivity of the pipe wall and \dot{Q} the heat flow from the hotter to the colder fluid through the pipe wall. The colored arrows represent the temperature level of the fluids, with blue representing colder temperature levels and red representing hotter levels. The bold black arrow shows the flow direction of the heat flow \dot{Q} .

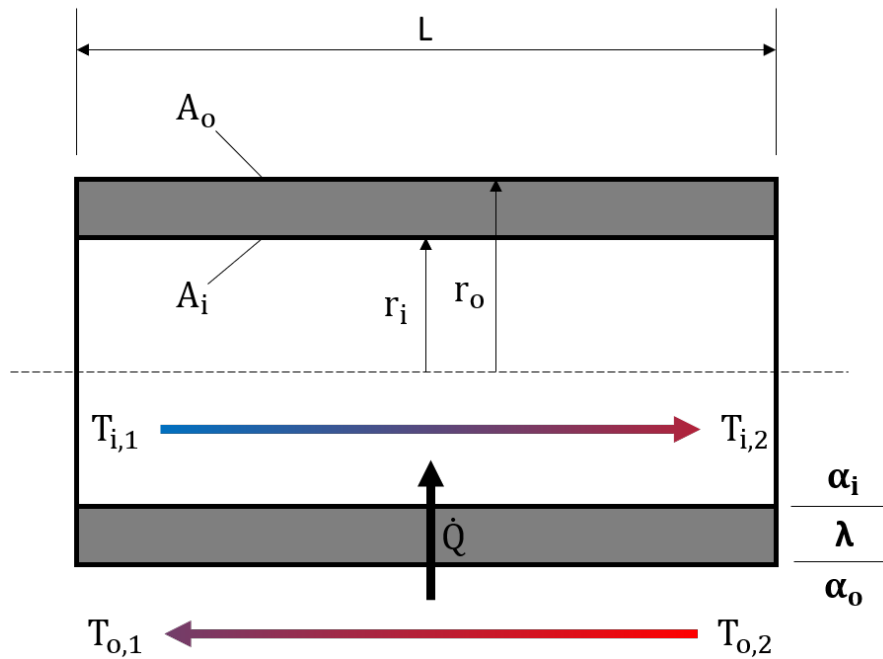


Figure 2.3: Heat transfer through a simple pipe

Convection

While the thermal conductivity λ is a fixed material-specific value, the heat transfer coefficient α changes with the flow conditions of the fluid streams. This subsection covers the heat transfer models for thermal convection of pipes and concentric annular ducts as shown in the VDI heat atlas [24] to calculate the heat transfer coefficient.

Dimensionless numbers

Dimensionless numbers are used to represent different conditions independent of the model size. The Reynolds number Re predicts flow patterns and specifies a fluid stream as laminar or turbulent. The Prandtl number Pr is the ratio of momentum to thermal diffusivity. The Nusselt number Nu is the ratio of convective to conductive heat transfer and is used to calculate the heat transfer coefficient α .

$$Re = \frac{v \cdot d_{\text{hyd}}}{\nu_{\text{vis}}} \quad (2.6)$$

$$Pr = \frac{\eta_{vis} \cdot c_P}{\lambda_f} \quad (2.7)$$

$$Nu = \frac{\alpha \cdot d_{hyd}}{\lambda_f} \quad (2.8)$$

In the equations above, v represents the fluid velocity, ν_{vis} the kinematic viscosity, η_{vis} the dynamic viscosity (with $\nu_{vis} = \eta_{vis}/\rho$), c_P the heat capacity and λ_f the thermal conductivity of the fluid. d_{hyd} represents the hydraulic diameter of the flow channel. For a non-circular channel, the hydraulic diameter is the diameter of a circular channel with the same flow conditions as the non-circular.

Convection in pipes

To simplify the heat transfer modulation a constant heat flow through the pipe wall and a hydrodynamically developed flow are assumed. The mean Nusselt number for the laminar case ($Re \leq 2300$) is given by equation 2.9.

$$Nu = \sqrt[3]{4.364^3 + 0.6^3 + (Nu_1 - 0.6)^3} \quad (2.9)$$

$$Nu_1 = 1.953 \cdot \sqrt{Re \cdot Pr \cdot \frac{d_{hyd}}{L}} \quad (2.10)$$

Equation 2.11 shows the calculation of the mean Nusselt number for turbulent streams ($Re \geq 10,000$). Equation 2.12 specifies the required friction factor ξ . The equations are only valid if $10^4 \leq Re \leq 10^6$, $0.1 \leq Pr \leq 1,000$ and $d_{hyd}/L \leq 1$.

$$Nu = \frac{(\xi/8) \cdot Re \cdot Pr}{1 + 12.7 \cdot \sqrt{\xi/8} \cdot (Pr^{2/3} - 1)} \cdot \left[1 + \left(\frac{d_{hyd}}{L} \right)^{2/3} \right] \quad (2.11)$$

$$\xi = (1.8 \cdot \log_{10}(Re) - 1.5)^{-2} \quad (2.12)$$

For the transition zone of Reynolds numbers between 2,300 and 10,000 the calculation of the mean Nusselt number is given as shown in equation 2.13. The required intermittency factor γ specifies equation 2.14. $Nu_{lam,2300}$ is the mean laminar Nusselt number for $Re = 2,300$ as shown in equation 2.9. $Nu_{tur,10000}$ is the mean turbulent Nusselt number for $Re = 10,000$ as shown in equation 2.11.

$$Nu = (1 - \gamma) \cdot Nu_{lam,2300} + \gamma \cdot Nu_{tur,10000} \quad (2.13)$$

$$\gamma = \frac{Re - 2300}{10^4 - 2300} \quad 0 \leq \gamma \leq 1 \quad (2.14)$$

Convection in annular ducts

To calculate the heat transfer coefficient of annular ducts, different equations for the mean Nusselt number are required. These are based on the assumptions of a hydrodynamically developed flow as well as constant and equal wall temperatures. Equation 2.15 is used for laminar flow conditions. The diameter ratio $b = d_i/d_o$ is calculated using the inner diameter of the outer tube d_o and the outer diameter of the inner tube d_i . For annular ducts the hydraulic diameter is $d_{\text{hyd}} = d_o - d_i$.

$$Nu = 3.66 + \left[4 - \frac{0.102}{b + 0.02} \right] \cdot b^{0.04} \quad (2.15)$$

Equations 2.16 to 2.20 provide the mean Nusselt number for turbulent flow conditions. The equations are only valid if $10^4 \leq Re \leq 10^6$, $0.6 \leq Pr \leq 1,000$ and $0 \leq d_{\text{hyd}}/L \leq 1$.

$$Nu = \frac{(\xi_{\text{ann}}/8) \cdot Re \cdot Pr}{k_1 + 12.7 \cdot \sqrt{\xi_{\text{ann}}/8} \cdot (Pr^{2/3} - 1)} \cdot \left[1 + \left(\frac{d_{\text{hyd}}}{L} \right)^{2/3} \right] \cdot F_{\text{ann}} \quad (2.16)$$

$$k_1 = 1.07 + \frac{900}{Re} - \frac{0.63}{1 + 10 \cdot Pr} \quad (2.17)$$

$$\xi_{\text{ann}} = (1.8 \cdot \log_{10}(Re^*) - 1.5)^{-2} \quad (2.18)$$

$$Re^* = Re \cdot \frac{[1 + b^2] \cdot \ln(b) + [1 - b^2]}{[1 - b]^2 \cdot \ln(b)} \quad (2.19)$$

$$F_{\text{ann}} = \frac{0.75 \cdot b^{-0.17} + 0.9 - 0.15 \cdot b^{0.6}}{1 + b} \quad (2.20)$$

The transition zone is calculated as shown in equation 2.13 and 2.14.

Heat transfer in packed columns

To calculate the heat transfer coefficient for a packed column flow α_{pack} , the characteristic length of the packing L_c is introduced.

$$L_c = d_{\text{pore}} \cdot \frac{\varepsilon^{1.5}}{1 - \varepsilon} \quad (2.21)$$

Thereby, d_{pore} represents the pore diameter of the packing or foam and ε represents the porosity of the packing or foam. In contrast to the Prandtl number, the Reynolds

and Nusselt numbers are calculated differently than shown above, as the following equations point out.

$$Re = \frac{v_{\text{pack}} \cdot L_c}{\nu} \quad (2.22)$$

$$Nu = \frac{\alpha_{\text{pack}} \cdot L_c}{\lambda_f} \quad (2.23)$$

Here, v_{pack} represents the fluid velocity through the packed bed, which can be calculated from the velocity v through a free flow cross-section and the porosity of the packing ε as equation 2.24 shows.

$$v_{\text{pack}} = \frac{v}{\varepsilon} \quad (2.24)$$

The heat transfer correlation for a flow through a packed bed is given by equation 2.25.

$$Nu = \left(0.5 \cdot Re^{0.5} + 0.2 \cdot Re^{\frac{2}{3}} \right) \cdot Pr^{\frac{1}{3}} \quad (2.25)$$

Particle heat transfer

To calculate the heat transfer coefficient of a solid moving bulk, Thanda [25] summarized a set of equations from Schlünder and Tsostas [24], [26] which will be presented in this subsection. The total heat resistance of the bulk consists of two individual resistances, as equation 2.26 shows. The first resistance is the contact resistance from the wall to the first particle layer α_{WS} . The second resistance is given by the bulk penetration resistance α_{SO} .

$$\frac{1}{\alpha} = \frac{1}{\alpha_{\text{WS}}} + \frac{1}{\alpha_{\text{SO}}} \quad (2.26)$$

Equation 2.27 specifies the calculation of α_{WS} .

$$\alpha_{\text{WS}} = \varphi \cdot \alpha_{\text{WP}} + (1 - \varphi) \frac{2 \cdot \lambda_{\text{gas}} / d_{\text{part}}}{\sqrt{2} + 2 \cdot (l_0 + \delta) / d_{\text{part}}} + \alpha_{\text{rad}} \quad (2.27)$$

Thereby, φ represents the surface coverage factor and α_{WP} is the heat transfer coefficient from the wall to the particle given by equation 2.28. λ_{gas} is the thermal conductivity of the interstitial gas, d_{part} is the diameter of the bulk particles, l_0 is the modified mean free path as given by equation 2.29, δ is the surface roughness of the particle and α_{rad} is the heat transfer coefficient from radiation as given by

equation 2.31.

$$\alpha_{WP} = \frac{4 \cdot \lambda_{\text{gas}}}{d_{\text{part}}} \left[\left(1 + \frac{2 \cdot (l_0 + \delta)}{d_{\text{part}}} \right) \cdot \ln \left(1 + \frac{d_{\text{part}}}{2 \cdot (l_0 + \delta)} \right) - 1 \right] \quad (2.28)$$

$$l_0 = 2 \cdot \frac{2 - \gamma}{\gamma} \left(\frac{2 \cdot \pi \cdot R \cdot T}{M_{\text{gas}}} \right)^{0.5} \frac{\lambda_{\text{gas}}}{p(2 \cdot c_{P,\text{gas}} - R/M_{\text{gas}})} \quad (2.29)$$

In equation 2.29 γ represents the accommodation factor as shown in equation 2.30 with C_{gas} as material specific constant, R is the universal gas constant, T and p are the average bulk temperature and pressure and M_{gas} and $c_{P,\text{gas}}$ are the molar mass and the specific heat capacity of the interstitial gas.

$$\log \left(\frac{1}{\gamma} - 1 \right) = 0.6 - \frac{(1000 \text{ K}/T) + 1}{C_{\text{gas}}} \quad (2.30)$$

$$\alpha_{\text{rad}} = 4 \cdot C_{W, \text{bulk}} \cdot T^3 \quad (2.31)$$

In the equation above, $C_{W, \text{bulk}}$ is the radiation coefficient given by equation 2.32.

$$C_{W, \text{bulk}} = \frac{\sigma_r}{(1/\epsilon_w + 1/\epsilon_{\text{par}} - 1)} \quad (2.32)$$

Here, σ_r is the black body radiation coefficient from Stefan-Boltzmann and ϵ_w and ϵ_{par} are emission coefficients for the wall and the bulk particles.

The following set of equations will show how the heat transfer coefficient to the bulk interior α_{SO} is calculated.

$$\alpha_{SO} = \frac{2\sqrt{\rho_{\text{bulk}} \cdot c_{P,\text{part}} \cdot \lambda_{\text{part}}}}{\sqrt{\pi} \cdot t_c} \quad (2.33)$$

Hereby, ρ_{bulk} is the density of the particle bulk, $c_{P,\text{part}}$ and λ_{part} are the specific heat capacity and heat conductivity of the bulk particles and t_c is the residence contact time, which is required for moving particle beds. Equation 2.34 shows how the contact time is calculated.

$$t_c = \frac{\rho_{\text{bulk}} V_{\text{bulk}}}{\dot{m}_{\text{part}}} \quad (2.34)$$

Thereby, V_{bulk} represents the volume of the total particle bulk and \dot{m}_{part} is the particle mass flow.

2.4 Reaction kinetics

Every system with constant boundary conditions strives towards an equilibrium state after the second law of thermodynamics. For a mixture of reactive components, these boundary conditions are temperature and pressure. The composition of the reactive mixture will change as long as the Gibbs energy of the mixture has not reached its minimum. After sufficient time, the reactions will stop and the equilibrium state of a reactive mixture is reached. Under constant boundary conditions, the equilibrium marks the maximum conversion a reaction can reach. Equation 2.35 indicates how the minimum of the Gibbs energy is calculated [27].

$$a(T, p, z) = - \sum_{i=1}^N \nu_i \mu_i = 0 \quad (2.35)$$

With a for the affinity, (T, p, z) for temperature, pressure and reaction conversion respectively, ν_i for the stoichiometric coefficient of component i and μ_i for the chemical potential of component i . The decomposition reaction of SO_3 is kinetically inhibited. To calculate the occurring conversion of an inhibited reaction, the reaction speed is required. The Arrhenius equation (equation 2.36) provides the reaction speed constant k as shown below.

$$k = k_0 \cdot e^{-\frac{E_A}{RT}} \quad (2.36)$$

$$\dot{n}_i = k \cdot c_i^n \cdot V_{\text{Rea}} \quad (2.37)$$

Equation 2.37 calculates the molar flow of component i as a result of a reaction of the order n , with c_i for the concentration of component i and V_{Rea} for the volume of the reaction zone. In equation 2.36, R represents the general gas constant. The kinetic parameters k_0 (pre-exponential factor) and E_A (activation energy) depend strongly on the reaction conditions and can be obtained by experimental results.

To enhance the inhibited decomposition of SO_3 , several catalysts were tested in the literature. Ishikawa et al. tested different metals and metal oxides [28]. They found out, that not only the well-known oxidation catalysts like platinum show good results but after reaching a higher temperature level the cheaper iron(III)-oxide (Fe_2O_3) can achieve the same conversion. Being able to use a cheaper catalyst is important when it comes to the economic validation of a process. This is why a lot of follow up research thematises Fe_2O_3 as catalyst for SO_3 decomposition ([32, 30, 34, 33, 29, 31]). Section 3.1 will explain the differences between the named research results and pick a kinetic equation that suits the set-up for this thesis. The downside of iron(III)-

oxide is its limited stability in combination with SO_3 . Fe_2O_3 and SO_3 form $\text{Fe}_2(\text{SO}_4)_3$ at sufficiently high SO_3 partial pressures and low temperatures. This reduces the usable catalyst mass and decreases its catalytic activity. To avoid this behavior a minimum temperature for the catalyst section has to be maintained. Guerra Niehoff for example suggests 900 - 950 °C for a reactor pressure between 10 - 20 bar [5].

2.5 Concentrated solar power system

A CSTE system utilizes solar irradiation to heat a heat transfer medium of a thermal power cycle. The utilization can be performed by different solar concentrators such as parabolic troughs, linear fresnel reflectors or heliostats. In comparison to the first two concentrators, heliostats focus the sunlight into a single point and are therefore able to reach significantly higher concentration levels [35]. The classical heliostat design has one or more mirror facets attached to a rigid support structure that can be moved relative to a fixed pillar. Figure 2.4 shows the typical T-shaped heliostat.



Figure 2.4: Heliostat on PSA in front and back view, courtesy of DLR/Ernsing [35]

The reflectivity of a heliostat is influenced by the used mirror surface quality and cleanness and by the surface shaping and mounting. The poorer the quality, the lower

is the reflective efficiency of a heliostat. The reflected radiation passes through the atmosphere and is weakened by the interactions with it. This effect is assumed by the atmospheric attenuation efficiency. As the purpose of a heliostat is to change the direction of a solar beam, the beam needs to be reflected apart from the surface normal. The larger the angle between the radiation entry and the surface normal gets, the lower is the effective reflective surface. This effect is called cosine efficiency, as the effective surface area is dependent on the cosine to the surface normal. Additional imaging errors are caused by the broadening of the focal point, as a result of the reflection of nonparallel sunbeams. As multiple heliostats reflect sunlight on the same area, super-positioning creates an intensity distribution at the focal area. Sectors with a lower intensity distribution keep unused and therefore cause the so-called intercept loss [36]. Direction errors caused by e.g. wind shaking the heliostats or non-perfect position calculations are demanded to be lower than 1 mrad, which means a heliostat in 1000 m distance will miss the aim point by less than 1 m [35]. In contrast to imaging errors, direction errors can be detected by cameras and corrected afterward.

Heliostats are positioned around a tower either staggered in rows or radially. For the placement of heliostats, a minimum distance needs to be considered to minimize losses through blocking or shading from neighboring heliostats. At the top of the tower, centered in the focal point, a solar receiver is placed. A receiver can work with different heat transfer media. For this thesis, bauxite particles are of interest, which can be heated by a so-called CentRec which is shown in figure 2.5.

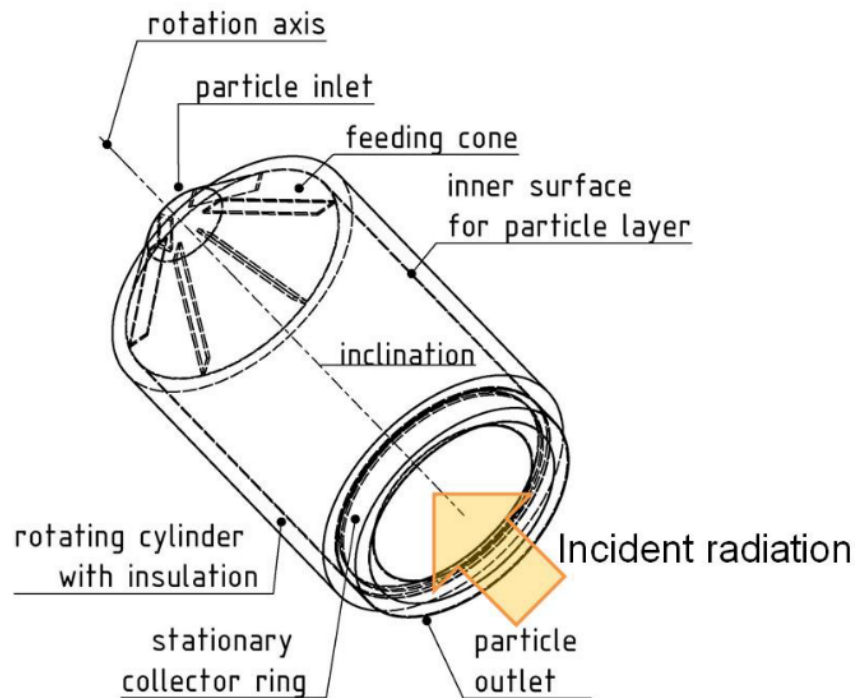


Figure 2.5: CentRec particle receiver design from Frantz [37]

The particles will develop a film inside the rotated receiver and are heated as they flow from the back to the front of the receiver, leaving the receiver right before the aperture area.

As the tower system can only produce heat during the daytime, a storage is needed, to guarantee longer process working hours. Therefore, the particles are stored in an insulated cylindrical tank. Heat losses are typically below 1 % in 3 h [38].

2.6 Economic analysis

To evaluate the financial sustainability of a process the investment and operating costs need to be analyzed. The cost calculations in this thesis are performed based on standardized cost accounting methods [39], [40]. To better compare different setups the weight specific costs are used. In this case, the Levelized costs of hydrogen (LCoH) are introduced, which level the investment and operating costs to the amount

of hydrogen producible as equation 2.38 shows.

$$\text{LCoH} = \frac{\text{CAPEX} \cdot \text{ANF} + \text{OPEX}}{\text{plant capacity factor} \cdot \text{annual hydrogen production}} \quad (2.38)$$

Thereby, CAPEX are the capital expenses which summarize all investment costs shown in equation 2.39, ANF is the annuity factor calculated as shown in equation 2.40, OPEX are the operating expenses shown in equation 2.41. The plant capacity factor and the annual hydrogen production will be introduced in section 3.3.

$$\text{CAPEX} = (1 + f_{\text{EPC}}) \cdot \sum_i C_i \cdot f_{\text{L},i} \quad (2.39)$$

The CAPEX include all investment costs that are required to buy a ready-to-use plant. To consider indirect costs (engineering, commissioning, contingencies) the EPC factor f_{EPC} is introduced. C_i are the investment costs of component i and $f_{\text{L},i}$ is the Lang factor to consider higher investments due to novel technology. The ANF is used to level the costs per year of owning and operating and is calculated using the operating time n and the interest rate j as shown below.

$$\text{ANF} = \frac{j \cdot (1 + j)^n}{(1 + j)^n - 1} \quad (2.40)$$

The OPEX can be separated into three groups as equation 2.41 shows.

$$\text{OPEX} = K_{\text{var}} + K_{\text{fix}} + K_{\text{rep}} \quad (2.41)$$

The first group is variable costs of the process, which are in this case the electricity costs. The second group is the fixed costs, which include insurance, maintenance and labor costs. The last group is the costs resulting from the regular replacement of plant components.

To calculate the investment costs for the novel particle thermal energy system, evaluations of Frantz were considered [41]. Equation 2.42 shows how the CentRec investment costs C_{rec} (in €) are calculated.

$$C_{\text{rec}} = \left[932,503 \cdot \left(\frac{D_{\text{cav}} + 0.2}{5.5} \right)^2 \cdot \frac{t_{\text{cav}}}{7.9} + 1000 \cdot \pi \cdot \left((D_{\text{cav}} + 0.2)^2 - (2 \cdot r_{\text{ap}})^2 \right) \right] \cdot 1.69 \quad (2.42)$$

Thereby, D_{cav} , r_{ap} and t_{cav} are geometry measurements of the CentRec as shown in figure 2.6.

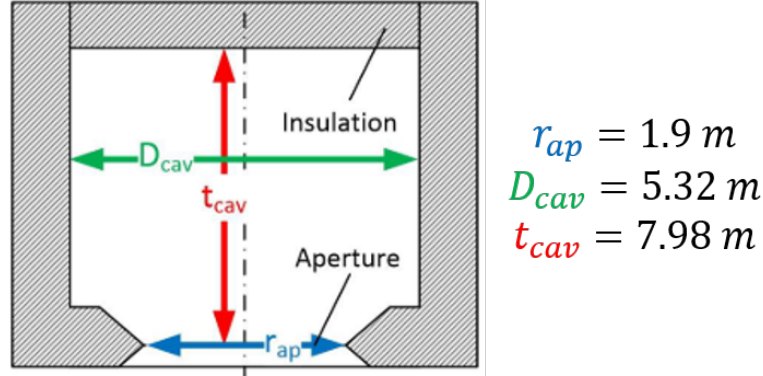


Figure 2.6: CentRec measurements optimised by Frantz for the 20 MW receiver [37]

To calculate the investment costs of the solar tower C_{tow} (in €), equation 2.43 is used.

$$C_{tow} = 161.7565 \cdot H_{tow}^{1.9274} \quad (2.43)$$

Here, H_{tow} is the tower height in meter. The investment costs of the thermal energy storage (TES) C_{TES} are calculated as shown in equation 2.44.

$$C_{TES} = C_{st} + C_{tr} + C_{par} \quad (2.44)$$

In this case, C_{st} (in €) are the investment costs for the thermal storage as shown by equation 2.47, C_{tr} (in €) are the investment costs for the transport system as shown by equation 2.46 and C_{par} (in €) are the particle investment costs as shown by equation 2.45.

$$C_{par} = 1.1 \cdot m_{par} \cdot C_{sp,par} \quad (2.45)$$

Here, m_{par} is the totally stored particle mass in the hot and cold storage. Another 10 % are added to account for particle in other components. $C_{sp,par}$ are the specific particle costs, which Belina quantifies to be $1 \frac{\text{€}}{\text{kg}}$ [42].

$$C_{tr} = 425,000 \cdot \left[1 + k_T \cdot \frac{T_l - T_{l,0}}{T_l} \right] \cdot \left[1 + k_m \cdot \frac{\dot{m} - \dot{m}_0}{\dot{m}} \right] \cdot \left[1 + k_H \cdot \frac{H_{tow} - H_{tow,0}}{H_{tow}} \right] \quad (2.46)$$

The scaling factors chosen by Frantz are $k_T = 0.1$, $k_m = 0.5$ and $k_H = 0.2$. T_l is the particle outlet temperature with $T_{l,0}$ being the reference design temperature of 600 °C . \dot{m} is the particle flow rate with \dot{m}_0 as reference design mass flow of $997 \frac{\text{kg}}{\text{s}}$. $H_{tow,0}$ is

the reference design tower height of 70 m. All reference design values were retrieved from Belina [42].

$$C_{st} = A_{st} \cdot C_{A,sp,is}(T_{hot}) + A_{st} \cdot C_{A,sp,is}(T_{cold}) \quad (2.47)$$

The temperature-dependent area-specific insulated structure costs $C_{A,sp,is}$ (in $\frac{\text{€}}{\text{m}^2}$) are calculated as shown by equation 2.48 using the factor $f_{is} = 0.3$ from Frantz [41]. A_{st} is the required containment surface area, calculated as shown in equation 2.49 using the particle density $\rho_{par} = 2,004 \frac{\text{kg}}{\text{m}^3}$ from Belina [42]. The temperatures of the hot and cold storage depend on the required particle temperature of the SAC and the particle temperature leaving the SAC.

$$C_{A,sp,is}(T_{st}) = 1,000 \cdot \left(1 + f_{is} \cdot \frac{T_{st} - 600}{400} \right) \quad (2.48)$$

$$A_{st} = \pi \cdot 2.5 \cdot \left(\frac{m_{par} \cdot 2}{\pi \cdot \rho_{par}} \right)^{\frac{2}{3}} \quad (2.49)$$

3 Modelling

The HyS-cycle is modeled using an Aspen Plus flowsheet containing all important process units. The used flowsheet was originally set-up by Bayer Botero [36] using a direct-irradiated reactor at ambient pressure. Guerra Niehoff [5] considered an indirect-irradiated concept at 15 bar with a focus on the SAC. Del Fabbro Acropinto [18] subsequently implemented Guerra Niehoffs concepts into Bayer Boteros flowsheet and improved the thermodynamic models. To implement a particle heated Bayonet reactor into the mentioned HyS flowsheet a detailed reactor model was created (section 3.1). The results of the detailed Bayonet model were then integrated into the HyS flowsheet (section 3.2). Subsequently, the CSTE was designed by using a program for heliostat field layout calculations (HFLCAL). For the techno economic analysis the performance of the solar tower receiver over the whole year was considered using Python (section 3.3).

3.1 Bayonet reactor model

The Bayonet reactor concept from SNL, presented in section 2.2, can be used in industrial scales and is therefore considered for the modulation. The used material is silicon carbide (SiC) because ceramic composite materials show good stability against corrosive substances like sulfuric acid under high temperatures. The dimensioning of the Bayonet reactor is taken from Binder [43] who was orientated towards the Westinghouse Electric reactor concept. Binder assumed that the Westinghouse Electric dimensioning works for the SNL concept as well. Figure 3.1 shows the measurements from Binder. It is assumed, that all flow paths are straight pipe flows and no tapering of the pipes occurs. The length of the reactor defines the amount of heat that is transferred and is therefore calculated dependently on the system. Binder set an upper limit of 10 m for the reactor length to stay within a producible scope.

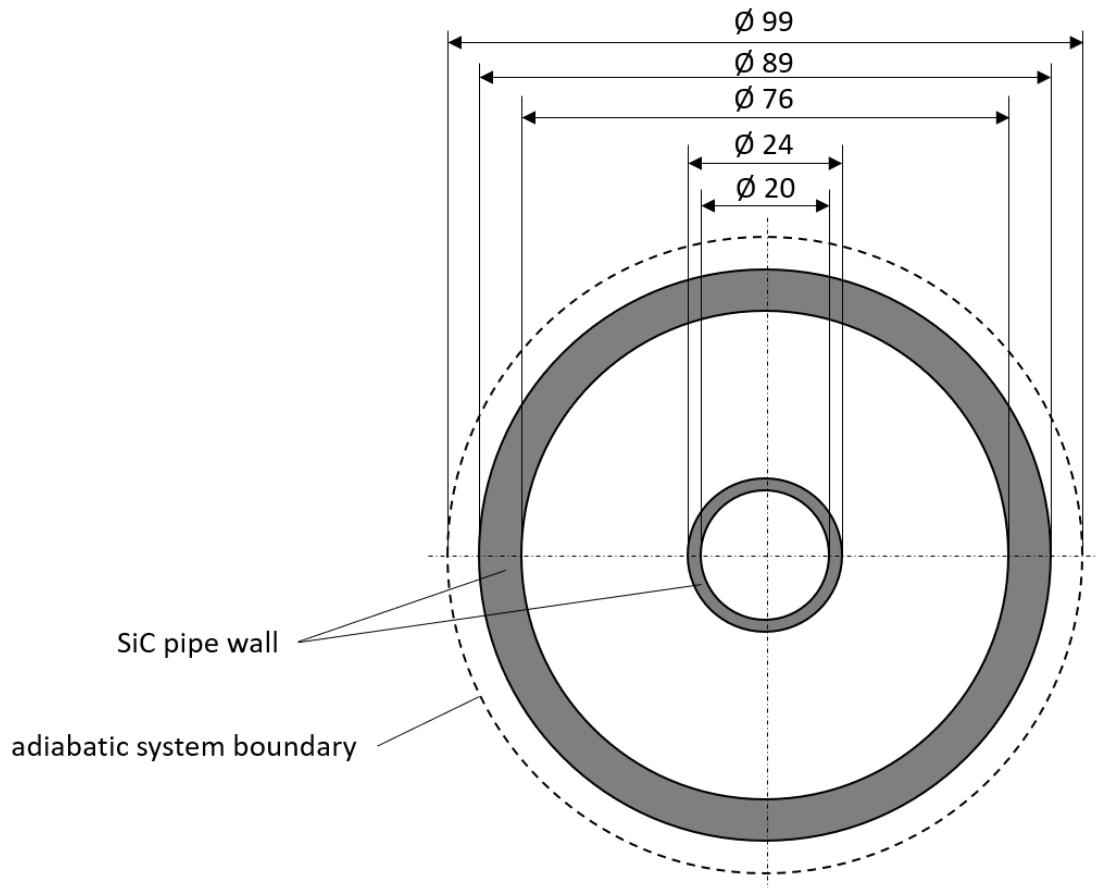


Figure 3.1: Measurements of the Bayonet reactor (in mm) from Binder [43]

The detailed reactor model is implemented using Python scripts that communicate with an simplified Aspen Plus model. The reactor is split lengthwise into three sections with approximately the same behavior under steady-state operating conditions. In the first section, the entering sulfuric acid is vaporized completely, the second section superheats the sulfuric acid vapor to the required temperature for the catalyst layer and dissociates the sulfuric acid to SO_3 . The third section is the catalytic layer for decomposition of SO_3 .

The sulfuric acid stream through the outer main channel of the reactor (main stream - MS) and the return flow through the inner pipe (counter stream - CS) are considered in two separated flow paths. The particle stream (PS) on the outside of the reactor is modeled as third separated flow path. Every length section of each stream is represented through one unit operation block in Aspen Plus. A discretization along the flow direction of each section is only required to depict dynamic reactor behavior, which is not considered in this thesis. This yields a demand of nine unit operation blocks,

which are shown in figure 3.2. The model consists of two types of unit operation blocks. All sections containing no catalytic enhanced reactions can be modeled using heater blocks, while the catalytic section of the decomposition is modeled using an RPlug reactor block. Python scripts are used to model the heat transfer through the reactor walls (subsection 3.1) between the different unit operation blocks.

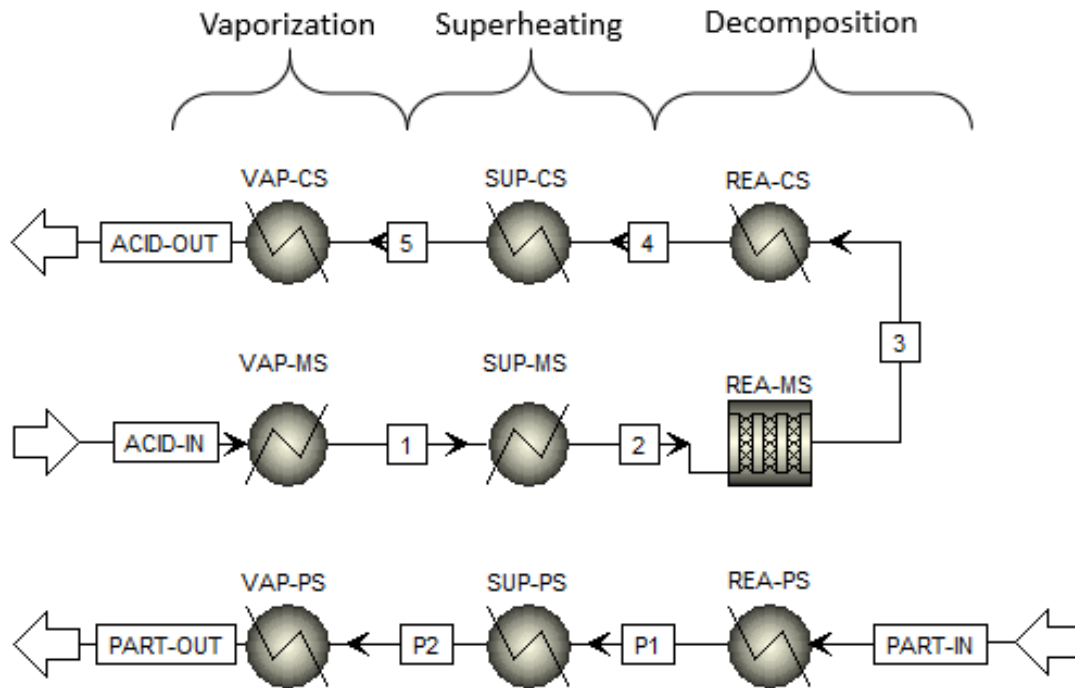


Figure 3.2: Aspen Plus Bayonet reactor model

The reactor inlet stream (ACID-IN) composition and state were taken from the HyS flowsheet of del Fabbro Acropinto. The heater blocks require two specifications to be solvable. One specification is the assumption that the reactor has no pressure drop. Comparable simulation results of Guerra Niehoff et al. have shown that the pressure drop for a reactor with 15 bar inlet pressure is lower than 2 % [5] and is therefore negligible. Corgnale et al. have simulated a pressure drop of approximately 10 % using higher throughputs and different geometries [44]. Thus, this assumption needs to be checked for different set-ups.

The second specification for the sulfuric acid inlet block VAP-MS is the above-mentioned condition to completely vaporize the sulfuric acid stream. For the following block (SUP-MS) the second specification is the temperature of stream 2, which is required to stabilize the used iron oxide catalyst in the next section. All other heater blocks

require the transferred heat duty as the second specification. This value is calculated by the heat transfer model of the Python scripts. The occurring reactions of the liquid and vaporized sulfuric acid are named in subsection 3.1. The RPlug block requires the specification of an external heat flux profile which is considered to be constant over the whole section length and is calculated by the Python scripts as well. It also requires the occurring reaction kinetic which will be explained in subsection 3.1.

Reaction system

Aspen Plus uses calculation methods with databases to calculate the required physical substance properties. As Gorensek et al. [9] have pointed out, the Oleum data package from Aspen Plus (Oleum is a mixture of SO_3 in sulfuric acid) only provides data up to $150\text{ }^\circ\text{C}$ and the pressure is limited up to 2 bar. The work of Mathias et al. removed these limitations [45]. Mathias refitted the Oleum modulation, but as the model tends to break down at higher temperatures, he introduced a second model for higher temperatures using the theoretical component "Ionpair" for the aqueous dissociation equilibrium of sulfuric acid. The downside of Mathias' model is that the miscibility gap between SO_2 and H_2O is not detected [18]. The model of Kaur et al. is able to detect the miscibility gap and can cover similar temperature ranges as the model of Mathias [46]. Therefore, this thesis uses the thermodynamic model of Kaur et al. [46]. To calculate the physical properties, the electrolyte Non-Random Two-Liquid (eNRTL) activity coefficients are used. The eNRTL calculation model is a standard approach to calculate the phase equilibrium of electrolyte mixtures. Kaur et al. deliver the required databases based on experiments and regressions.

In the vapor phase, only SO_2 , H_2SO_4 , H_2O and SO_3 can exist. In the liquid phase, electrolyte reactions may occur. Figure 3.3 summarizes the components and reactions considered by the Kaur model. Studies by del Fabbro Acropinto concluded, that the databases for the ternary system ($\text{H}_2\text{SO}_4\text{-H}_2\text{O-SO}_3$) are valid for temperatures between 0 and $500\text{ }^\circ\text{C}$. The databases for the binary system ($\text{H}_2\text{O-SO}_2$) are valid for temperatures between 0 and $120\text{ }^\circ\text{C}$ as pointed out by Kaur. These temperature ranges are sufficient enough for the chosen reactor pressure of 15 bar.

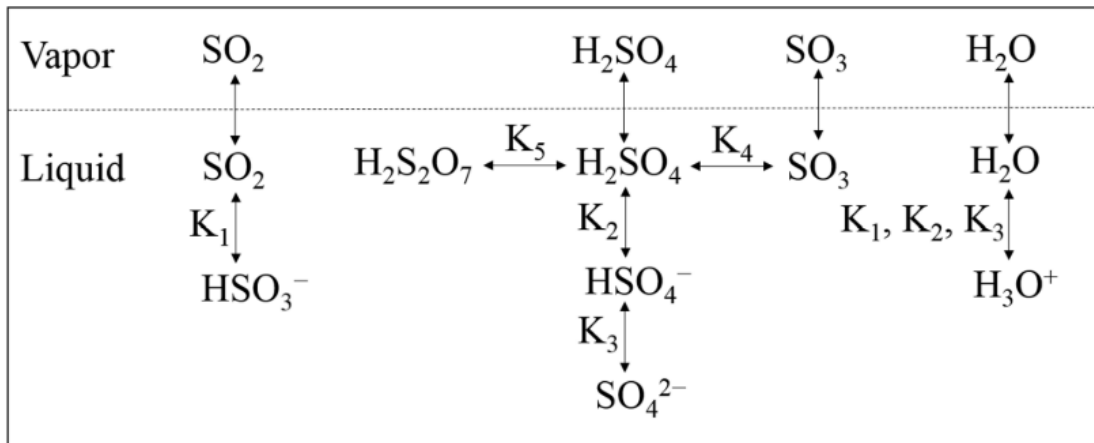
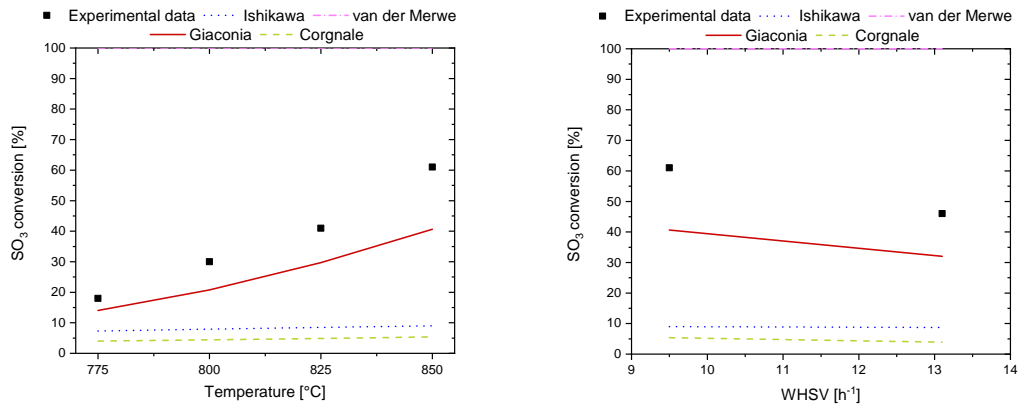


Figure 3.3: Oleum reaction model considered by Kaur [46]

The vapor phase in the Bayonet reactor will be superheated to temperatures over 800 °C where most of the gaseous sulfuric acid is dissociated to H_2O and SO_3 . To model the subsequent inhibited decomposition of SO_3 , kinetic reaction parameters in accordance with section 2.4 are required. The kinetic parameters depend on the catalyst material as well as on the shape and size of the catalyst particles. The Bayonet reactor can be filled with a loose filling of pure iron oxide particles with diameters of 1 - 2 mm. Choosing smaller particle diameters increases the amount of catalyst per square meter, but also will increase the pressure drop over the filling. This catalyst filling corresponds to experimental data gathered by Giaconia et al. [34]. To find the best fitting kinetic parameters, different modulations were checked with the experimental data from Giaconia as figure 3.4 shows.



(a) Temperature dependency (WHSV $\approx 10 \text{ h}^{-1}$) (b) WHSV dependency (Temperature = 850 °C)

Figure 3.4: Reaction kinetic tests with experimental data from Giaconia [34] for kinetic parameters by Ishikawa [28], van der Merwe [31], Giaconia [34] and Corgnale [47] at 1 bar

Giaconia used four different catalyst particle types for his experimental studies. For this thesis only the set-up with pure iron oxide particles with 1-2 mm diameter are of interest. Experimental data from 1 to 4 bar at different temperatures and weight hourly space velocities (WHSV) are available. Figure 3.4 shows a comparison to the experimental data for 1 bar. The other pressure investigations showed similar results and are not discussed further. Giaconia mentioned, that no influence of the pressure on the conversion could be observed for the considered range of 1-4 bar. The WHSV of a reactor can be calculated as shown in equation 3.1.

$$WHSV = \frac{\dot{m}_{\text{H}_2\text{SO}_4}^{\text{in}}}{m_{\text{cat}}} \quad (3.1)$$

With $\dot{m}_{\text{H}_2\text{SO}_4}^{\text{in}}$ representing the mass flow of sulfuric acid and m_{cat} the used catalyst mass. To reproduce the experimental data using different kinetic parameters, the Aspen Plus unit operation block RPlug was used. All required information for the simulation set-up can be taken from Giaconia, except the catalyst bed voidage. The bed voidage was calculated considering an ideally packed filling with identical, spherical particle without inner pores. The real bed voidage is expected to be higher because of an unideal packing behavior and will be checked in a following sensitivity analysis.

As the results of figure 3.4 show, only the kinetic parameter found from Giaconia can represent the kinetic behavior for the chosen catalyst type. The results from Ishikawa and Corgnale underestimated the SO₃ conversion, which could be caused by the different set-ups as both used platin-coated alumina catalyst particles instead of dense iron

oxide particles. The kinetic parameter from van der Merwe calculated a conversion of 100 % for all points and therefore exceeded the experimental SO_3 conversions. The reason for that could be the fine iron oxide powder van der Merwe used, which has a larger surface area and therefore higher activities than the particles of Giaconia. Thus, the kinetic parameters of Giaconia were taken for further considerations. Figure 3.5 shows the sensitivity analysis for the calculated bed voidage on the left side. For the sensitivity analysis, the ideal bed voidage value of 0.54 was increased (+ 50 % curve) and decreased (- 50 % curve) by 50 %. It can be seen, that the expected higher bed voidage of a real packing can represent the experimental data. Resulting in a mean relative error of 6.8 % for the increased bed voidage of approximately 0.80.

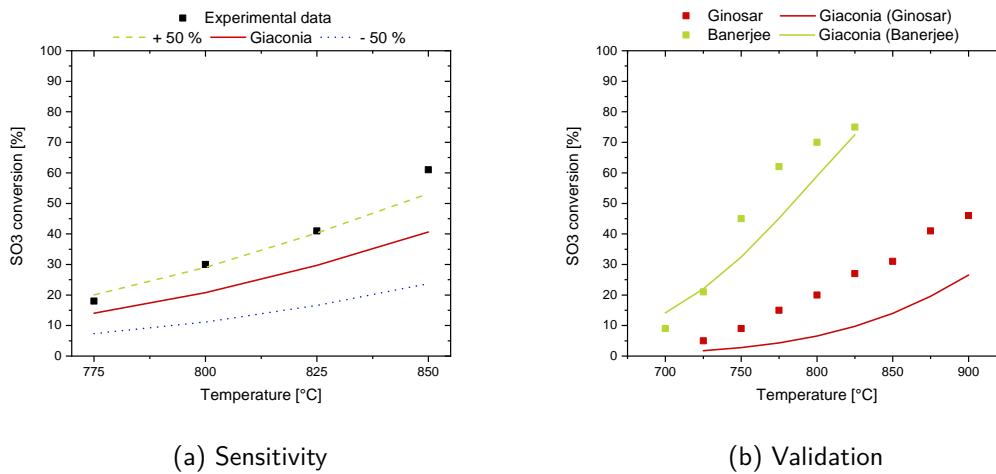


Figure 3.5: (a) Sensitivity check for calculated catalyst bed voidage and (b) Validation of found kinetic parameters with different experimental set-ups by Ginosar [32] and Banerjee [33] for 1 bar

Figure 3.5b shows the test of the kinetic parameters by simulating under different experimental conditions from Giaconia, such as the temperature, the flowrate or the used amount of catalyst. The figure shows the experimental data of Banerjee [33] and Ginosar [32] coupled with the simulation results using the kinetic of Giaconia with an increased bed voidage of 0.8. The set-up of Banerjee with a larger catalyst size (4-6 mm diameter) can be reproduced better, than the set-up of Ginosar with a finer powder (0.1-1.9 mm). These results show once again how dependent the kinetic parameters are on the used catalyst type. The found kinetic parameters are shown in table 3.1.

Table 3.1: Kinetic parameter for SO₃ decomposition from Giaconia [34]

Name	pre-exponential factor k_0 [$\frac{\text{kmol}}{\text{N h}}$]	k_0^* [$\frac{1}{\text{h}}$]	activation energy E_A [$\frac{\text{kJ}}{\text{mol}}$]
Value	$\frac{F_{\text{SO}_3}^0}{p_{\text{SO}_3}^0 \cdot V_{\text{Rea}} \cdot WHSV} \cdot k_0^*$	3.00E+08	162.6

The pre-exponential factor from Giaconia is calculated dependently on the molar inlet flow rate of SO₃ ($F_{\text{SO}_3}^0$), the inlet partial pressure of SO₃ ($p_{\text{SO}_3}^0$), the reaction volume, the WHSV and a catalyst specific factor k_0^* as table 3.1 shows. The simulation start up script from Python calculates the pre-exponential factor based on the simulation settings and passes it to the Aspen Plus model.

The Bayonet model calculated a SO₃ conversion of 98 % for a reactor pressure of 15 bar and a reaction zone temperature between 925 to 950 °C using the kinetic parameter from Giaconia. The equilibrium conversion for these boundary conditions is 83.7 %. This means, that the kinetic parameters exceed the maximum possible conversion and are not valid for the boundary conditions required in this thesis. The reason for that is, that the set-up of this thesis can reach equilibrium conversion rates and the pre-exponential factor from Giaconia is only valid for a system sufficiently far away from equilibrium conversions. Ishikawa noted, that for space velocities (SV) below 10,000 $\frac{1}{\text{h}}$ the SO₃ decomposition reaches equilibrium conversions for all tested catalyst materials. The space velocity as a fraction between the volumetric flow rate and the catalyst bed volume of the set-up in this thesis is 3,090 $\frac{1}{\text{h}}$ for 800 °C and 1,893 $\frac{1}{\text{h}}$ for 925 °C catalyst inlet temperature. These are the two found Bayonet configurations of this thesis which will be shown in section 4.1. Therefore, the two Bayonet configuration models will calculate equilibrium conversion rates using the Gibbs energy approach presented in section 2.4. Set-ups with higher flow rates or smaller reactor pipes need to consider the kinetic parameter from Giaconia.

Heat transfer model

To simulate the heat transfer through the pipe walls, additional Python scripts are required. The calculation is split into three sections, one for every reactor section. As there are multiple reciprocal conditions for the heat transfer in each reactor section,

iterative algorithms are used to find the solution for the given simulation parameter. The basic idea of the heat transfer model is to calculate the length of each section and to specify the heat distribution between the counter and the particle stream, as both transfer heat into the main stream. Therefore, the term split factor is introduced, which is calculated as shown in equation 3.2.

$$\text{split factor} = \frac{\text{heat flux counter stream}}{\text{total heat flux}} \quad (3.2)$$

Equation 2.5 is used to calculate the heat transfer area for a known heat flux \dot{Q} , thermal transmittance U and temperature difference. With the given geometry from figure 3.1, the section length can be calculated from the heat transfer area. For every reactor section, two heat transfer areas have to be calculated. One area is calculated for the heat transfer from the counter stream and another from the particle stream. The basic procedure of the Python scripts is to change the split factor until both section lengths have the same value. Calculating the same length for both transfer areas means that the selected split factor is the true distribution of the heat fluxes and the calculated section length is necessary to guarantee the required total heat flux to the main stream. Part of the heat transfer Python scripts is the calculation of the overall thermal transmittance as shown in section 2.3. Figure 3.6 presents the algorithm behind the first section calculation in Python - the calculation of the reaction section.

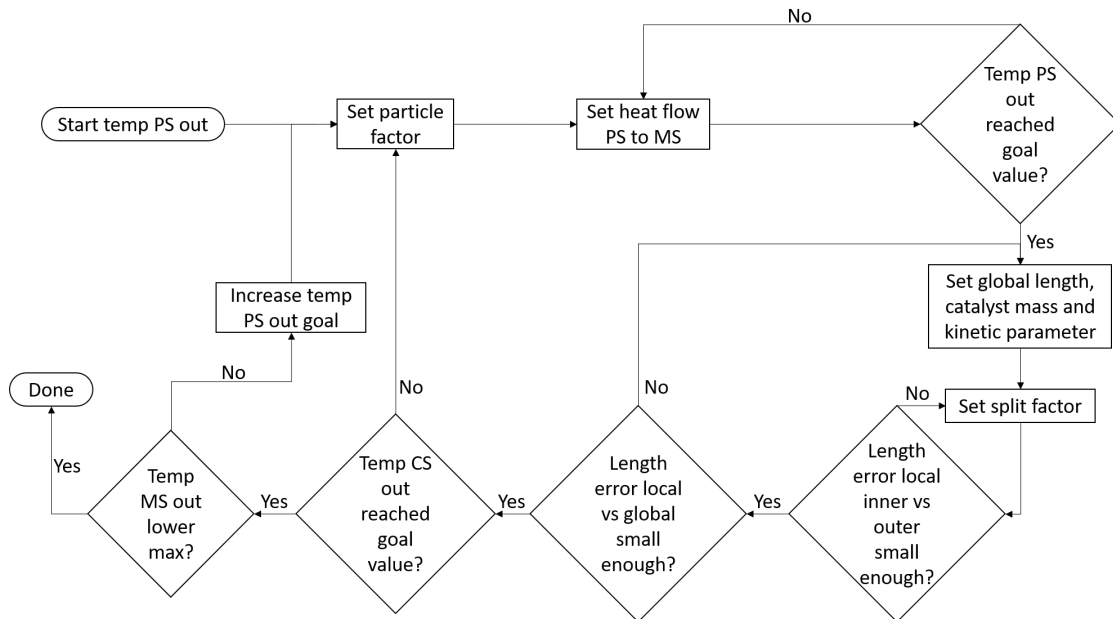


Figure 3.6: Simplified algorithm flowchart for heat transfer calculations of reaction section in Bayonet model

The script starts with a temperature goal for the outlet temperature of the particle stream, correspondingly to figure 3.2 the temperature of stream P1. The starting goal value is the temperature of stream 2 plus the minimal temperature difference which is required to guarantee heat transfer. Table 4.2 shows the used minimal temperature differences. In the next step, a particle factor is selected. The particle factor is the fraction of particle mass flow to sulfuric acid mass flow through the reactor. With the known particle flow rate (flow rate of stream PART-IN), the transferred heat in block REA-PS is corrected until the goal temperature of stream P1 is reached. In the next step, the section length of the reaction section is estimated and all corresponding parameters (catalyst mass and kinetic parameter) are set. The length needs to be guessed because the RPlug block requires a section length to be specified. The guessed length value, called global length in the script, will be checked and corrected later on. The next step is to calculate the split factor as described above. The received section length called local length in the script, is subsequently compared to the guessed global length. If these values do not match, the calculated local length is used as the new guessed global length and the calculation starts again until the difference between local and global length is small enough. Afterwards, the outlet temperature of the counter stream - the temperature of stream 4 - is checked. The goal temperature here is the temperature of stream 2 plus the minimum temperature as well. If the goal temperature

is not reached, the particle factor is corrected. A smaller temperature than the goal temperature means, more particles are required, as the fraction of heat coming from the particles needs to be increased and vice versa for a higher temperature. If the goal temperature of stream 4 is reached, the final check is for the temperature of stream 3. This temperature is the maximum reactor temperature, which must always be lower than the particle inlet temperature minus the minimum temperature difference. If this condition can not be fulfilled, the goal temperature for stream P1 will be increased by 3 K and the whole calculation process needs to start again. The temperature increase of 3 K was chosen as compromise between computing time and accuracy. If that increase of the goal temperature is necessary, the assumption that the particles can transfer the maximum possible amount of heat at the given temperature difference was wrong. It needs to be noted, that in most of the cases and especially in the two final reactor concepts this assumption was true. The script has many intermediate queries to check if the continuation of a loop is necessary to improve the calculation time. For a better overview, these queries are not integrated into the flowchart. As a result of that script, streams 3, 4, P1 and PART-In are completely determined. The two following scripts for the superheating and the vaporization section only need to calculate the split factor and the section length as described above and are therefore not thematized in more detail.

The iterative procedure used by the Python scripts is the numerical bisection method. The method uses an upper (a) and a lower bound (b), the target value ($c = (a + b)/2$) is the midpoint between these boundaries. After every iteration, the upper or the lower bound gets corrected, dependently on the results of an error function of the target value $f(c)$. The accuracy of this method is set by the goal value of the error function $f(c)$ and the minimum and the maximum number of iterations. The most bisectional iterations were set to be precise up to the third decimal.

The calculation of the overall thermal transmittance from section 2.3 needs further model-specific additions which should be named here. One addition is the consideration of two-phase regions as they occur in the vaporization section. The main stream is vaporized and the counter stream is condensed. Both phenomena influence the heat transfer coefficient in the corresponding stream. To model the influence correctly, a discretization of the vaporization section would be required to check at which point each stream has a certain phase equilibrium. Additionally, does the consideration of two phases require a more complex heat transfer description as shown in section 2.3. As Binder has simulated the same reactor geometry with the required discretization, his

calculated heat transfer coefficient is taken for the inner heat transfer if condensation and vaporization occur. The mean heat transfer coefficient of Binder is approximately $283 \frac{\text{W}}{\text{m}^2\text{K}}$ for a sulfuric acid flow rate of $21.4 \frac{\text{kg}}{\text{h}}$. As the sulfuric acid flow rate influences the heat transfer coefficient as well, this is only an approximation to the real heat transfer coefficient. If the counter stream is not condensed, only the heat transfer coefficient of the main stream is influenced. In that case and for the calculation of the outer heat transfer to the particle stream in the vaporization section, an approach of Thanda is used [25]. He noticed that the increased heat transfer coefficient of a two-phase stream is not noticeable, as the lower heat transfer coefficient of the particle stream or the thermal conductivity of the wall limits the overall thermal transmittance more. In that cases, the heat transfer coefficient of the two-phase stream is simply not considered when calculating the overall thermal transmittance.

The second addition is the consideration of packings in all sections with a gaseous stream. As Connolly has investigated, using packings in the Bayonet tubes, the total heat transfer can be increased and the required reactor length is lowered [48]. Binder has tested different packing types and recommended the usage of a packing foam with a pore diameter of 5 mm and a porosity of 0.9 for the best ratio of heat transfer increase to a generated pressure drop when used for gaseous streams [43]. Therefore, this packing type is used for the Bayonet configurations of this thesis. Table 3.2 summarizes the required parameter for the packed column heat transfer calculations as shown in subsection 2.3.

Table 3.2: Parameter for packed column heat transfer calculations

Model section	Filling type	Diameter d_{pore} [m]	Porosity ε [-]
SUP-MS	metallic foam	0.005	0.9
REA-MS	catalyst material	0.002	0.8

Table 3.3 and table 3.4 give the required parameter for the calculation of the heat transfer coefficient of the particle layer on the shell side of the Bayonet tube as shown in subsection 2.3 taken from Belina [42].

Table 3.3: Parameter for the calculation of α_{WS}

Name	Symbol	Value
surface coverage factor	φ	0.8
particle diameter	d_{part}	0.001 m
particle surface roughness	δ	0
molar mass air	M_{gas}	0.0289583 $\frac{\text{kg}}{\text{mol}}$
material constant	C_{gas}	2.8
emission coefficient wall	ϵ_{W}	0.1
emission coefficient particle	ϵ_{par}	0.8
specific heat capacity air	$c_{\text{P, gas}}$	calc. from Belina [42]
thermal conductivity air	λ_{gas}	

Table 3.4: Parameter for the calculation of α_{S0}

Name	Symbol	Value
particle bulk density	ρ_{bulk}	2184 $\frac{\text{kg}}{\text{m}^3}$
bulk width	-	0.005
spec. heat capacity particle	$c_{\text{P, part}}$	calc. from Belina [42]
thermal conductivity particle	λ_{part}	

As no experimental data for a particle-heated Bayonet reactor at the reference configuration of this thesis exist, no complete validation of the model was possible. Nevertheless, each part of the Bayonet model was validated with a suitable comparison. To validate the inner heat transfer calculations between the counter and the main stream, the simulation results from Binder were used [43]. As Binder simulated an air-heated Bayonet reactor, the outer heat transfer to the particle layer was validated using simulation results from Belina [42]. For both cases, the Bayonet model was changed to replicate the exact simulation set-ups, including reactor geometry, packing considerations, inlet composition and state, reactor temperature, pressure and inner mass flow.

The model was able to replicate the simulation results of Belina completely, which is not surprising, as the same calculation scripts for the particle heat transfer model were used. The results of Binder for the calculation of a packed column flow could also be replicated. The results for an unpacked flow were underestimated by 44 %, which may be caused by the simplified approach to discretize the reactor in three main sections, instead of discretizing each section locally as Binder has simulated his reactor. As the final reactor model considers packed column flow only, the underestimation is neglected.

3.2 Scale-up and flowsheet integration

Combined usage of a solar-powered HyS-cycle with a flash furnace copper production is of interest because both cycles require similar chemicals. The advantage of a HyS-cycle integration into an existing copper smelting process is the provision of green hydrogen as environmentally friendly fuel while additionally producing the for the flash furnace required oxygen. This section will cover the integration possibilities for the copper production at Olympic Dam in Australia run by the BHP Group.

The yearly production rate on site was 9,674,000 tons of ore in 2007. The ore does not only contain copper but also silver, gold and uranium which are all enriched on-site as well [49]. The ore is crushed and separated into copper- and uranium-rich parts by flotation. The copper slurry is dried and fed to the flash furnace with a concentration of approximately 40 % [50]. The flash furnace requires fuel and oxygen, which will react with the iron and sulfur in the copper concentrate and melt the copper through excess reaction heat. The impure molten copper will be enriched and refined using electrorefining methods. The contained sulfur was oxidized to sulfur dioxide and leaves the furnace with the off-gas. Afterwards, the sulfur dioxide will be converted to sulfuric acid in an acid plant. It can be seen, that besides hydrogen and oxygen, sulfur dioxide and sulfuric acid are components of the HyS-cycle too. Therefore, existing logistics to provide these chemicals can be used or even replaced. This thesis however will concentrate only on the integration of hydrogen and oxygen.

The ore mined in 2007 resulted in a production of 170,000 tons of refined copper [49]. The company published plans in 2009 to increase the production of up to 750,000 tons of copper per year [51]. As newer articles report, the current plans are to increase the production of up to 300,000 tons of refined copper per year [52]. The current production method requires liquefied petroleum gas (LPG) and fuel oil to run different

furnaces. These two fossil fuels can be replaced with green hydrogen to reduce the amount of emitted CO₂. It is assumed, that the modification of the furnaces only requires nozzles to guarantee that the flow rate is higher than the burning rate of hydrogen [53]. The resulting hydrogen demand is calculated using the lower heating value of all fuels, as the combustion water in the furnaces will always be gaseous (flash furnace off-gas temperature: 1,000 °C [54]). The oxygen demand for the production capacity of 2007 was 122,000 tons per year [55]. To scale the HyS-cycle, either the occurring hydrogen demand or the oxygen demand can be satisfied. Table 3.5 summarizes three possible HyS-cycle scales, that will be investigated in this thesis.

Table 3.5: Olympic Dam integration scenarios

Scenario	Copper production [$\frac{t}{a}$]	Demand satisfied	Hydrogen produced [$\frac{t_{H_2}}{a}$]	Production rate (HyS) [$\frac{t_{H_2}}{a}$]
1	170,000	hydrogen	8,347	25.07
2	300,000	hydrogen	14,730	44.23
3	300,000	oxygen	27,126	81.46

It is assumed, that the demand of the 300,000 tons of copper scenarios scale linear to the 170,000 tons scenario. To calculate the production rate of the HyS plant, it was assumed that the plant will be shut down on 32 days per year. This results in a production time of 7,992 hours per year.

To integrate the model of the particle-heated Bayonet reactor into the HyS Aspen flowsheet, a hierarchy block was used. The hierarchy block functions as a black box model representing a cluster of particle-heated Bayonet reactors. A figure of the complete Aspen flowsheet can be found in the Appendix A. Figure 3.7 shows the section of the complete HyS flowsheet of sulfuric acid concentration and SAC.

the Bayonet cluster. Stream 6 is dissolved using the property model of Kaur presented earlier on [46]. Therefore, the DISSOLVING hierarchy block was implemented, which reverses the dissolution reactions of Kaur and outputs a stream SOUT only consisting of sulfuric acid and water. The information of that stream can be used by the Python script to set the required concentration heat correctly. As the Python script used iterative methods to approach the required conditions (same mass flux in stream 6 and 10 and SOUT sulfuric acid concentration of 80 wt.-%), the final HyS flowsheets have small errors for the mass and concentration settings, which are summarized in table 3.6. The relative errors were calculated as a fraction of the deviation to the goal value. The table also includes the so-called acid factor for each flowsheet, which represents the fraction of sulfuric acid streaming through the Bayonet cluster and hydrogen being produced. This factor is used for the solar dimensioning in the next section (section 3.3).

Table 3.6: Characteristics of the final HyS Aspen flowsheet for both Bayonet reactor model concepts

Model type	Bayonet tubes required [-]	Relative mass flow error [%]	Relative concentration error [%]	Acid factor $[\frac{\text{kg}_{\text{acid}}}{\text{kg}_{\text{hydrogen}}}]$
925 °C	1,521	0.17	0.13	77.33
800 °C	1,111	0.04	0.11	75.29

The requirements for the product quality are different from the requirements del Fabbro Acropinto fulfilled. The quality of oxygen is oriented towards the oxygen plant used at Olympic Dam, which generates 92-99.95 vol.-% oxygen at 0.8-2 bar gauge [50]. As del Fabbro Acropinto needed purer oxygen on higher pressure levels, the oxygen purification from his flowsheet was not required and is removed (see complete flowsheet in Appendix A). The quality demand of hydrogen is not specified, but to guarantee clean combustion, the contamination needs to be minimal. The required pressure of hydrogen depends on the storage facility. As hydrogen is produced in the amount consumed by the furnaces, only small intermediate storage is required. The product stream of hydrogen in the original flowsheet is 100 vol.-% hydrogen at 15 bar. It is assumed to fulfill the requirements and no changes are made.

3.3 Solar system dimensioning

The first step of dimensioning the solar system is to design the tower system including the heliostat field, the solar tower and the receiver. The design process was performed using the DLR software HFLCAL. Table 3.7 summarizes the required settings to start the HFLCAL field optimization. Important for further calculations is the Direct Normal Irradiance (DNI), as only this part of the total solar irradiation can be harnessed by concentrating solar systems [56].

Table 3.7: HFLCAL required input

Name	Value	Unit
Latitude	-30	°
Height above sea level	107	m
Design time	21. March 12:00	
Design DNI	831	$\frac{W}{m^2}$
Aperture type	circular	
Aperture radius	1.9	m
Design flux	1,900	$\frac{kW}{m^2}$
Receiver power at design point	21.5	MW
Receiver efficiency (design)	0.94	

The latitude and height above sea level are chosen for the location Olympic Dam. The design date of 21. March is chosen, because it is a moderately irradiated time. For the southern hemisphere, the 21. December is the best irradiated design point and the 21. June is the lowest irradiated design point. By choosing a moderately design point a steadier performance of the field throughout the year is guaranteed. The design DNI is taken from the available DNI data of Olympic Dam at the design time. The receiver specific settings are taken from Frantz, who performed an optimization of the used 20 MW CentRec [37]. The receiver design power is calculated by dividing the nominal receiver power of 20 MW by the receiver efficiency. The heliostats of the company BrightSource Energy were taken as a reference for the tower system design. Figure 3.8

shows the dimension and characteristics of that heliostat.

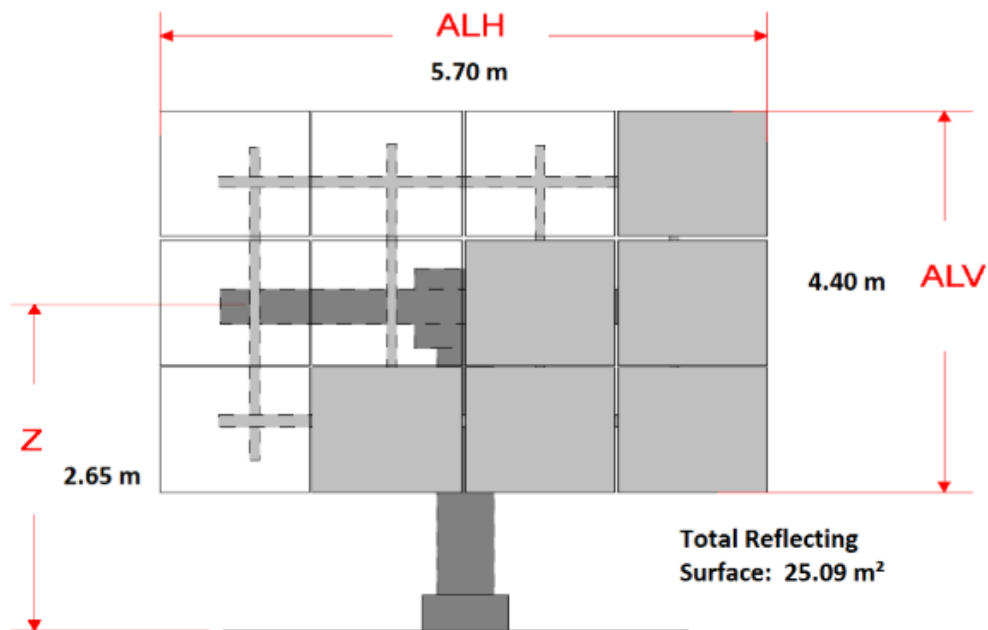


Figure 3.8: Dimensions for BrightSource Energy heliostat [57]

The heliostat has four facets with a mirror reflectivity of 87 % and a beam error of 3.3 mrad. Subsequently, HFLCAL will optimize the heliostat placement, the tower height and the aperture tilt angle dependently on the chosen settings. To design the field, clear sky irradiances for the chosen location are used. Figure 3.9 shows the found tower system and table 3.8 summarizes all important information about it.

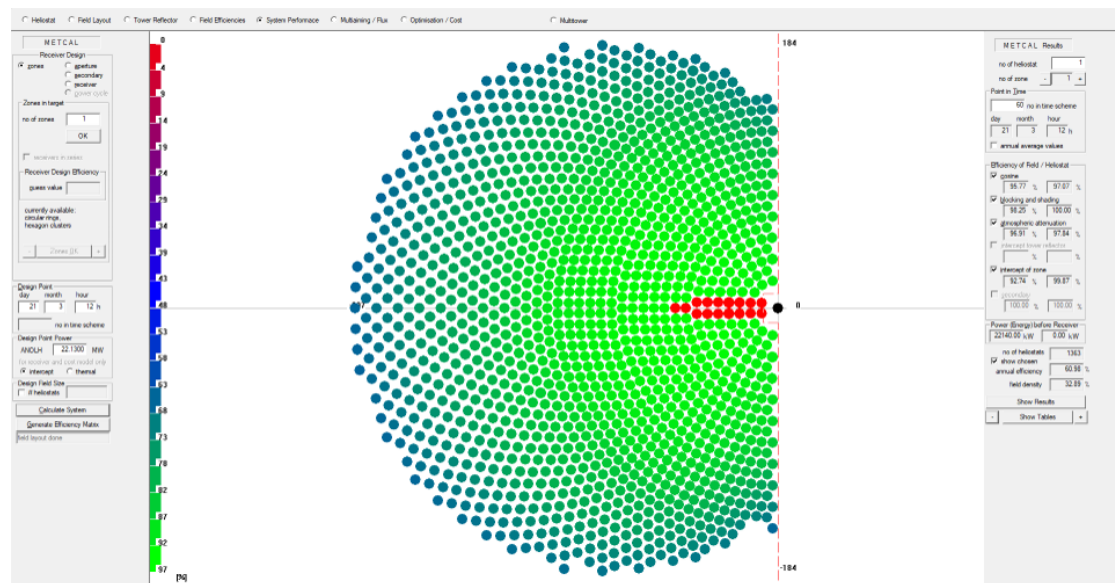


Figure 3.9: HFLCAL final tower system

The black dot in the coordinate origin symbolizes the solar tower. The heliostats are visualized by their efficiency at the design time. The aperture is oriented in a southbound direction and no heliostats are placed in the northern field behind the tower.

Table 3.8: HFLCAL final tower system

Name	Value
Number of heliostats	1363
Tower height	135.7 m
Aperture tilt angle	46.6 °
Cosine efficiency	0.88
Reflectivity	0.87
Blocking & shading efficiency	0.91
Atmospherical attenuation	0.97
Intercept efficiency	0.92

The efficiencies, as explained in section 2.5, are calculated as yearly average by HFLCAL and are shown to give an understanding of the composition of the total tower system efficiency for the found set-up. To calculate the time discretized performance, HFLCAL provides data of the optical efficiency (total heliostat field efficiency) as a function of the solar altitude. To calculate the solar altitude, the mathematical model of the Astronomical Almanac was used as presented by Michalsky [58]. It was tested by Michalsky to have an accuracy of 0.01 degree until at least 2050. The model calculates the azimuth and elevation for every point in time and location on earth required. Figure 3.10 shows on the left side the calculated optical efficiency of the heliostat field at 1st of January 2022 using the solar altitude.

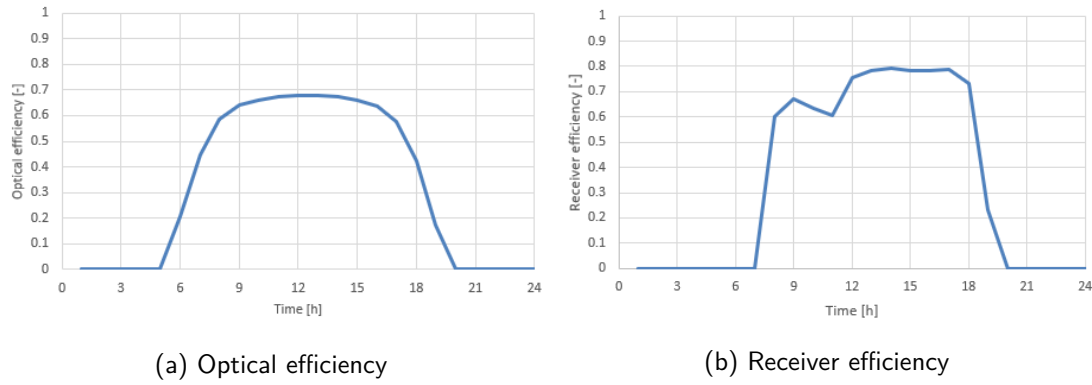


Figure 3.10: Tower system efficiencies at 1st of January 2022

The right side of figure 3.10 shows the resulting receiver efficiency on 1st of January 2022. The efficiency drop starting at 9 o'clock is caused by a lower DNI value around that time, probably caused by clouds. Equation 3.3 gives the calculation method for the CentRec efficiency η_{rec} introduced by Buck [59].

$$\eta_{rec} = \beta - \left(\epsilon \cdot \sigma_r \cdot T_{rec,out}^4 + h \cdot (T_{rec,out} - T_{amb}) \right) \cdot \frac{1}{P''_{apt}} \quad (3.3)$$

Thereby, $\beta = 0.95$ is the absorptivity, $\epsilon = 0.9$ is the emissivity, $\sigma_r = 5.67E-08 \frac{W}{m^2K^4}$ is the Stefan–Boltzmann constant, $T_{rec,out} = 1,100 \text{ } ^\circ\text{C}$ is the particle outlet temperature of the receiver, $h = 30 \frac{W}{m^2K}$ is the heat loss coefficient and $T_{amb} = 300 \text{ } ^\circ\text{C}$ is the ambient temperature. P''_{apt} is the solar flux density on the aperture, which is calculated hourly by the Python script by multiplying the optical efficiency with the DNI value. The DNI values, despite the calculated solar altitude, are measured values of the year 2005. The yearly irradiation in Olympic Dam of 2005 was approximately $2,558 \frac{kWh}{m^2}$. The total tower system efficiency is calculated by multiplying the two efficiencies. Table 3.9 gives

the mean annual efficiencies as calculated by the Python script.

Table 3.9: Tower system annual efficiencies

Name	Value
Optical efficiency	54.3 %
Receiver efficiency	70.9 %
Total efficiency	38.5 %

The simulation of the particle storage throughout the year is calculated by Python scripts as well. The script needs the specific heat capacity for bauxite particles, which equals to $1,230 \frac{\text{J}}{\text{kg K}}$ - taken from the Aspen property data bank. It requires the temperatures of the particles entering and leaving the receiver and the particle factor. These values can be taken from table 4.2. To be able to calculate the particle flow rate from the required hydrogen demand, the introduced acid factor is needed. This value can be taken from table 3.6. The annual hydrogen demand changes for the three introduced scenarios in table 3.5. As there are two types of Bayonet configurations that can be used for the three production size scenarios, the scenario list needs further specification as shown in table 3.10.

Table 3.10: Summary of considered solar powered HyS scenarios

Scenario	Copper production [$\frac{\text{t}}{\text{a}}$]	Demand satisfied	Bayonet configuration	Hydrogen produced [$\frac{\text{t}_{\text{H}_2}}{\text{a}}$]	Production rate (HyS) [$\frac{\text{t}_{\text{H}_2}}{\text{d}}$]
1a	170,000	hydrogen	925 °C	8,347	25.07
1b	170,000	hydrogen	800 °C	8,347	25.07
2	300,000	hydrogen	925 °C	14,730	44.23
3a	300,000	oxygen	925 °C	27,126	81.46
3b	300,000	oxygen	800 °C	27,126	81.46

Table 3.11 shows the heat demand of the HyS plant for every scenario presented above.

The thermal power demand of scenarios using the 800 °C configuration is lower than comparably sized scenarios using the 925 °C configuration because the specific heat demand of the 800 °C Bayonet reactor is lower.

Table 3.11: Required thermal power of HyS plant for each scenario

Scenario	Required thermal power [MW]
1a	64.19
1b	54.26
2	113.27
3a	208.60
3b	176.32

The Python script starts with calculating the required particle flux to supply the HyS plant. The storage size is calculated dependently on the set time to guarantee full load operations. A storage size of 12 h e.g. can maintain the particle flux for 12 h without new particles being heated by the tower systems. Besides the storage size, the so-called solar multiple (SM) is a setting value too. The SM is the fraction of the installed nominal solar power to the required power of the supplied system. In this thesis the installed nominal solar power equals the number of tower systems times 20 MW nominal power of a single tower system and the required power of the supplied system is the energy demand of the SAC section in the HyS plant. Winter stated, that for a large storage and a $SM > 2.4$, 24-hour operations - as required in this thesis - are possible [60].

If the solar system is not able to provide enough solar energy to heat the required particle flux, it is assumed that the particles are heated by switching on an additional heater. Therefore, 24-hour full load operation of the HyS plant is guaranteed. To measure the proportion of solar supplied HyS production, the plant capacity factor is introduced. The plant capacity factor indicates the fraction of time in the year at which the HyS plant is only supplied by the solar tower systems. Therefore, the Python script calculates an energy balance for the particle storage for every hour in the year. If this energy balance gets negative, more particles are required than supplied or stored and additional heating would be necessary. To optimize the plant capacity, the script

searches for the best time to shut down the HyS plant. Therefore, the lowest irradiated coherent 32 days are determined. The particle storage energy balance on these days is zero, as no particles are produced or required. The mentioned heat loss of the storage system is considered in the energy balance as well. Figure 3.11 gives an impression of how the Python script works.

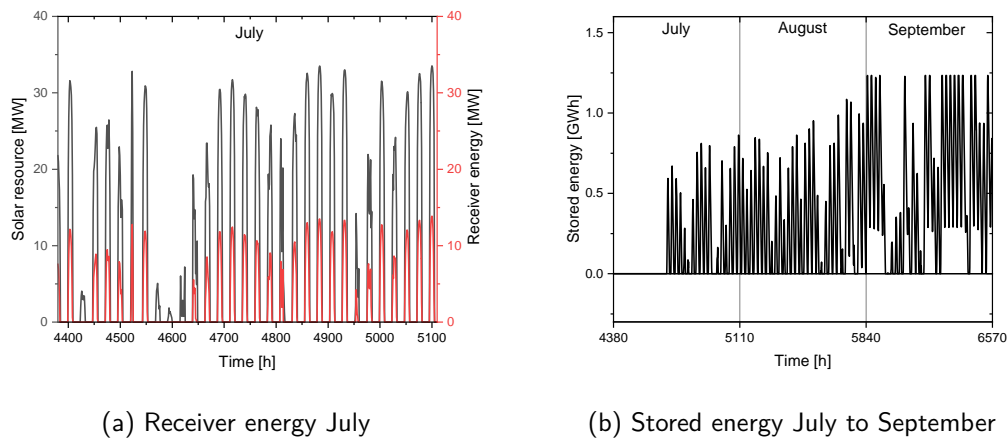


Figure 3.11: Storage system performance for $SM = 4.6$, storage size = 19 h, scenario 1a

Figure 3.11a shows the solar resource in black. The solar resource is the solar energy that is irradiated onto the total heliostat area. By multiplying the solar resource with the total tower system efficiency, the receiver energy (shown in red) can be calculated. It can be seen, that the irradiation on some days is not high enough to generate any receiver energy. The month of July is one of the lowest irradiated months in Australia, as figure 3.11b will demonstrate. The right figure shows the results of the accumulated energy balance of the storage system for the months July to September. The first weeks of July, additional to the last weeks of June, are calculated to be the lowest irradiated 32 days. Therefore, the plant was shut down and no energy is stored in the particle storage. The selected storage time of 19 h for the production rate of scenario 1a equals a storage size of 1.23 GWh. As the image shows, only the irradiation as of September can fill the particle storage. These months shown in the right image have a high demand for additional particle heating overnight. Approximately every time the stored energy curve reaches the value zero, additional heating is required. The total plant capacity of that configuration is 81.6 %.

Table 3.12 summarizes important assumptions for the cost calculations as described in section 2.6.

Table 3.12: Summary of assumptions for LCoH calculations

Name	Value	Unit	Source
Heliostat price	85	$\frac{\text{€}}{\text{m}^2}$	[57]
EPC	33	%	[5]
Land costs	2	%	[57]
Hydrogen selling price	1.57	$\frac{\text{€}}{\text{kg}}$	[61]
Operation time	25	years	[41]
Interest rate	7	%	[41]
Electricity price	30.85	$\frac{\text{€}}{\text{MWh}}$	[62]
Insurance rate	2	%	[5]
Maintenance	4	%	[5]
Labour costs	130,000	$\frac{\text{€}}{\text{a}}$	[63], [14], [64]
Replacement interval	10	years	[65]

The heliostat price ($100 \frac{\text{USD}}{\text{m}^2}$) was conceived from the company BrightSource energy [57]. The before mentioned currency conversion factor for USD was used to calculate the price of approximately $85 \frac{\text{€}}{\text{m}^2}$. The EPC factor was taken from Guerra Niehoff [5] who chose 33 % of the CAPEX based on comparable process challenges. The receiver investment costs are excluded by calculating the EPC investment as the calculations from Frantz already include indirect costs for the receiver [41]. The land costs were taken from Rosenstiel [57], who named 2 % of the total CAPEX. The hydrogen selling price is adopted from the report of Hinkley et al. [61]. They named a price range of 1.50-2.50 $\frac{\text{AUD}}{\text{kg}}$. Considering the currency conversion and the inflation, a selling price of $1.57 \frac{\text{€}}{\text{kg}}$ was chosen. The operation time and interest rate were taken from Frantz et al. [41] as they considered a 20 MW CentRec system as well. The electricity price is conceived from a report by Brinsmead [62] who observed the Australian electricity market. Considering the demand for a carbon dioxide tax, they named an electricity price of approximately 50 $\frac{\text{AUD}}{\text{MWh}}$ for the year 2021. Considering the currency conversion an electricity price of $30.85 \frac{\text{€}}{\text{MWh}}$ was chosen. The insurance rate and maintenance costs were received from Guerra Niehoff [5] who named 2 and 4 % of the total CAPEX.

The labour costs were taken from a report of Pitz-Paal [63] who chose 48,000 $\frac{\text{€}}{\text{a}}$ per worker for a conception in Spain in 2005. Considering the inflation [14] and the payment difference between Spain and Australia [64], 130,000 $\frac{\text{€}}{\text{a}}$ per worker were chosen. The replacement interval of 10 years was taken from Guerra Niehoff [5].

The calculations of the Bayonet and the SDE investment costs are taken from Corgnale et al. [15]. The inflation adjustment to the year 2015 was made by Guerra Niehoff [65]. An additional inflation adjustment to the year 2021 was made by del Fabbro Acropinto [18]. The investment costs are dependent on the daily produced amount of hydrogen mentioned in table 3.10. Guerra Niehoff chose a Lang-factor of 1.44 for the Bayonet reactor and 1.2 for the SDE investment costs which are used here as well. The investment costs of the gas separation and the vacuum system are taken from del Fabbro Acropinto which depend on the daily hydrogen production of the plant as well. For both systems, a Lang-factor of 2 was selected. Additionally, a Lang-factor of 2 is selected for the receiver and a factor of 1.5 for the TES to compensate the novel designs for the 1,100 °C configuration.

4 Results and Discussion

This chapter will summarize the results gathered from the different modulation levels. Starting with the section introducing the found Bayonet reactor configurations (section 4.1) and closing with a section summarizing the complete HyS system and validating the economical efficiency of all scenarios (section 4.2).

4.1 Bayonet Configurations

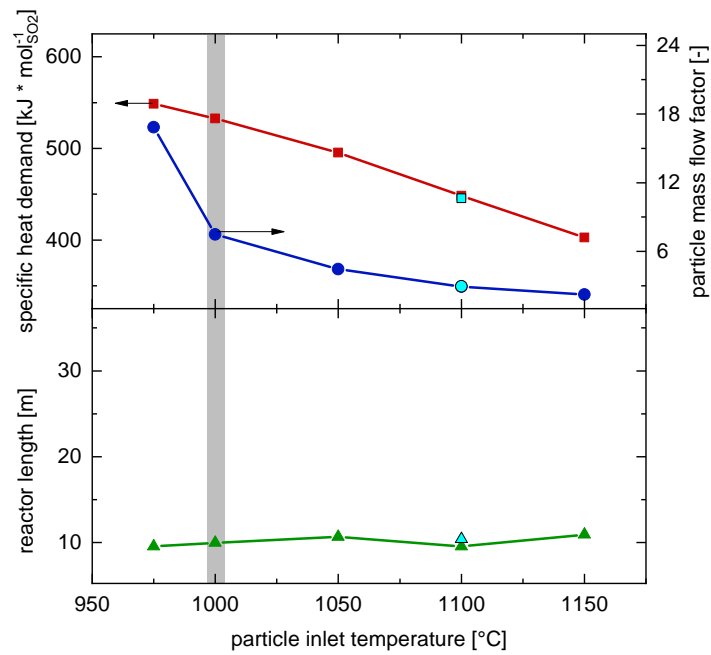
The Bayonet model presented in section 3.1 can calculate results for different settings. To validate the influence of different parameter settings, a reference set-up is introduced. Table 4.1 summarizes all relevant parameter for the reference set-up.

Table 4.1: Bayonet model reference set-up

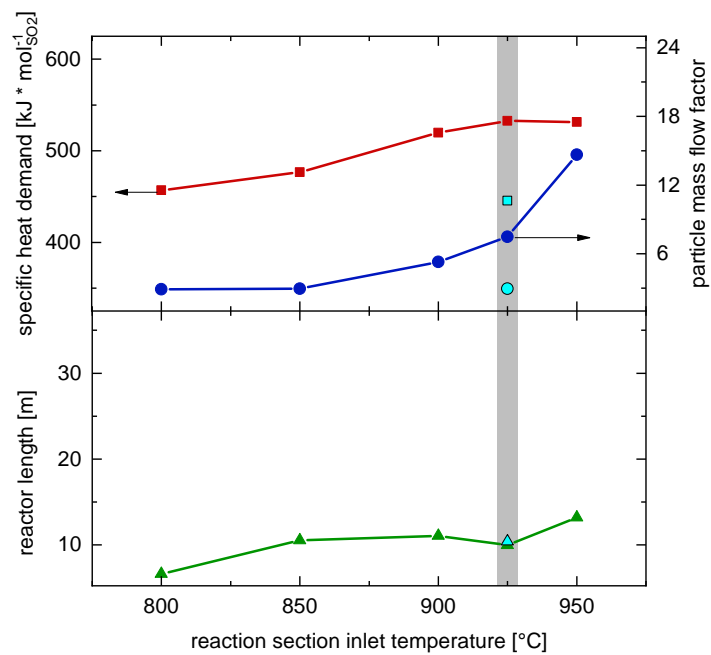
Name	Value
Reactor pressure	15 bar
Catalyst inlet temperature	925 °C
Sulfuric acid flow rate	25 $\frac{\text{kg}}{\text{h}}$
Particle inlet temperature	1,000 °C
Packing consideration	only SUP-MS packed

As Guerra Niehoff has observed, a Bayonet reactor pressure of 15 bar can reduce the specific heat demand of the HyS-cycle and simplifies the integration of the Bayonet reactor into the overall process [5]. Thus, a reactor pressure of 15 bar is chosen for

all configurations. For a reactor pressure of 15 bar the catalyst temperature needs to be at least 925 °C to avoid inactivation reactions [5]. Binder evaluated the influence of the sulfuric acid flow rate on the reactor configuration [43]. He suggested a flow rate of 21.4 $\frac{\text{kg}}{\text{h}}$ for a reactor pressure of 10 bar. With a higher pressure of 15 bar the flow rate can be increased to replicate the same flow conditions in the reactor. Therefore, the reference flow rate is 25 $\frac{\text{kg}}{\text{h}}$. The used bauxite particles are currently able to perform well up to temperatures of 1,000 °C, as Buck et al. have noted [59]. Therefore, the reference inlet temperature of the particle stream is 1,000 °C. As mentioned in earlier chapters, the superheating section of the main stream for the reference case is filled with a packing foam to increase the heat transfer. For the catalyst inlet temperature, the sulfuric acid mass flow, the particle inlet temperature and the packing consideration, a parameter study was performed. Figure 4.1 shows the impact of the both varied temperatures.



(a) Particle inlet temperature



(b) Reaction section inlet temperature

Figure 4.1: Parameter study for a) the particle inlet temperature and b) the reaction section inlet temperature, the reference case is highlighted in gray, the optimised case is represented with turquoise symbols.

The figure shows the impact of the varied temperature on the specific heat demand in red, the particle mass flow factor in blue and underneath, the impact on the calculated total reactor length is shown. The gray highlighted area symbolizes the reference state. For all parameter performance improving values are chosen which are summarised in table 4.2. The results of the improved set-up are shown with turquoise symbols. The left image of figure 4.1 shows the impact of the particle inlet temperature. With an increasing particle temperature, the particle mass flow factor is lowered. This is caused because the total temperature difference between the sulfuric acid main stream and the particle stream in the reaction section is increased with a hotter particle stream. Therefore, the particle stream can transfer more heat per particle mass. As the hotter particle stream is transporting more heat additionally, lesser particles are required and the particle mass factor declines. With lesser particles on the outside, more heat is recovered from the counter stream. This effect is shown in the decrease of the specific heat demand of the Bayonet reactor for hotter particle temperatures. A significant effect on the total reactor length is not observed. As the positive effect of an increased particle temperature reaches a flattening at approximately 1,100 °C, this temperature is chosen for the improved Bayonet set-up. It is assumed, that a more improved bauxite particle or a different particle material can handle the hotter temperature. The effect of that new technology is considered with higher costs in the techno-economic analysis, as section 4.2 will show. The right image of figure 4.1 shows the impact of the reaction section inlet temperature. The observed improvement on the specific heat demand and the particle mass factor with an increased temperature difference in the reaction section can be observed here as well. The effect is reciprocally shown by decreasing the inlet temperature. As the currently used iron oxide catalyst requires a minimum inlet temperature of 925 °C, this value is also chosen for the improved set-up. As the turquoise symbols indicate, the improvement of other parameters is already able to decrease the specific heat demand and the particle factor significantly in comparison to the reference case. As a comparable set-up of Guerra Niehoff considered the possibility of an inlet temperature of 800 °C with the assumption, that future catalyst materials can stay active at that temperature level, a second improved set-up is introduced [5]. These two set-ups will be summarized and compared later on. The total reactor length is slightly increased with an increasing reaction section inlet temperature. This is mainly caused by the increased superheating section length. To superheat the sulfuric acid to higher temperatures a larger heat transfer area is required and therefore, the section length is increased.

Figure 4.2 shows the impact of different packing scenarios. The three considered

packing-scenarios are 1) no additional packing, 2) a packing foam in section SUP-MS and 3) a packing in every vapor reactor section. These packing-scenarios do not impact the consideration of the influence of the catalyst packing in section REA-MS. Besides the packing consideration, no values of the reference case are varied.

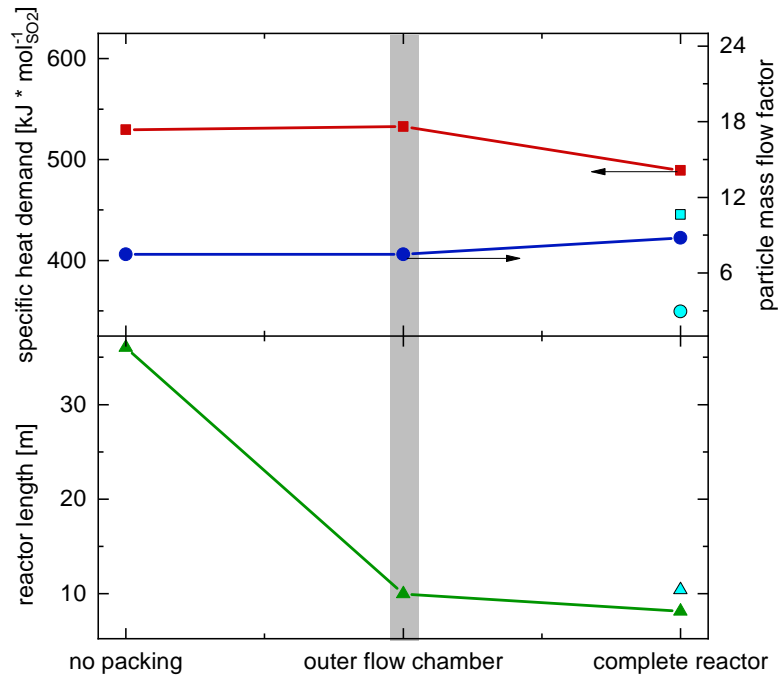


Figure 4.2: Parameter study for different packing-scenarios, the reference case is highlighted in gray, the optimised case is represented with turquoise symbols.

With the increased heat transfer in the superheating section of the main stream in packing-scenario 2, the total reactor length can be decreased significantly in comparison to packing-scenario 1. This is caused because the main stream is laminar and shows low heat transfer coefficients. Increasing the heat transfer into the main stream lowers the required heat transfer area and therefore, the reactor length. To fill the complete reactor with a packing foam in packing-scenario 3 does not decrease the total reactor length significantly. A positive effect of the complete reactor packing can be noted for the specific heat demand. As packing-scenario 3 lowers the specific heat demand, a complete reactor packing is considered for the improved set-up, as the turquoise symbols indicate. The last parameter study was carried out for the sulfuric acid mass flow through the reactor as figure 4.3 shows.

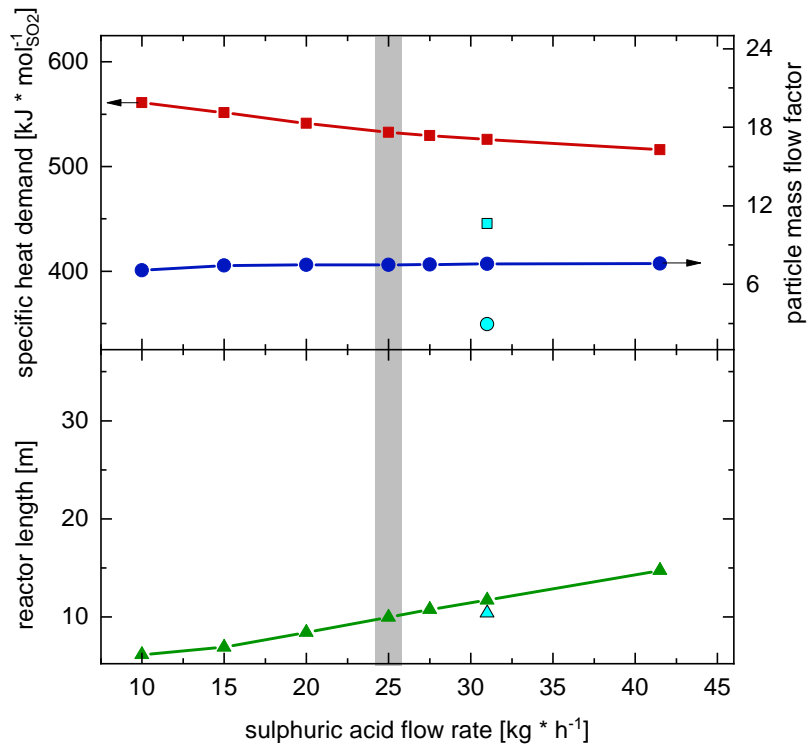


Figure 4.3: Parameter study for sulfuric acid mass flow rate, the reference case is highlighted in gray, the optimised case is represented with turquoise symbols.

A higher mass flow rate through the Bayonet reactor increases the turbulence of the sulfuric acid stream and therefore the heat transfer inside the reactor. With a higher heat transfer inside the reactor, more heat can be recovered from the inner counter stream, which causes a slight decrease in the specific heat demand for higher sulfuric acid fluxes. An impact on the particle mass flow factor is not observed. Additionally to the decreased specific heat demand, the reactor length is increased with higher fluxes. This is caused because more sulfuric acid requires more transferred heat to reach the same temperatures and conversions. To be able to transfer more heat, a larger heat transfer area is required and therefore, the reactor length is increased. To finally improve the 925 °C set-up, the sulfuric acid mass flow rate is increased until a total reactor length of 10 m is reached as the turquoise symbols indicate. Thereby, the producible range of Binder is maintained and the specific heat demand is lowered to a possible minimum. The same procedure was carried out for the 800 °C set-up, which can be seen in table 4.2 where both set-ups are compared. There, the mentioned parameter Catalyst inlet temperature, Particle inlet temperature, Packing consideration

and Sulfuric acid flow rate are optimized as shown by the parameter study above.

Table 4.2: Bayonet model final set-ups comparison

Name	925 °C set-up	800 °C set-up
Reactor pressure [bar]	15	15
Catalyst inlet temperature [°C]	925	800
Particle inlet temperature [°C]	1,100	1,100
Packing consideration	complete reactor	complete reactor
Minimum temperature difference [K]	5	50
Reactor length [m]	10.41	9.98
Particle factor [-]	2.96	2.28
Specific heat demand [$\frac{\text{kJ}}{\text{mol SO}_2}$]	446	377
SO ₃ conversion [%]	81.1	83.2
Max. reactor temperature [°C]	949	969
Particle outlet temperature [°C]	305	182
Sulfuric acid outlet temperature [°C]	346	265
Sulfuric acid flow rate [$\frac{\text{kg}}{\text{h}}$]	31	41.5

To simulate the 925 °C configuration, a minimum temperature difference of 5 K was used. The 800 °C configuration required an increased minimum temperature difference of 50 K to have feasible solution from Aspen. It can be seen, that the particle factor of the 800 °C case is lower which increases the amount of heat that is recovered from the counter stream and explains the lowered specific heat demand. As the maximum reactor temperature of the 800 °C scenario is higher, a higher SO₃ conversion is reached. The higher sulfuric acid flow rate in an identically long reactor requires more heat, which explains the lower outlet temperatures of the particle and the sulfuric acid stream. As seen, the 800 °C set-up performs better than the 925 °C set-up, but it only is a theoretical consideration that is not feasible today.

As explained in section 3.2, these two reactor configurations were used to create two

HyS flowsheet configurations in Aspen Plus. Subsequently a pinch analysis was carried out for each configuration, to identify the heat demand of the complete HyS-cycle excluding the particle heated SAC. Figure 4.4 shows the results.

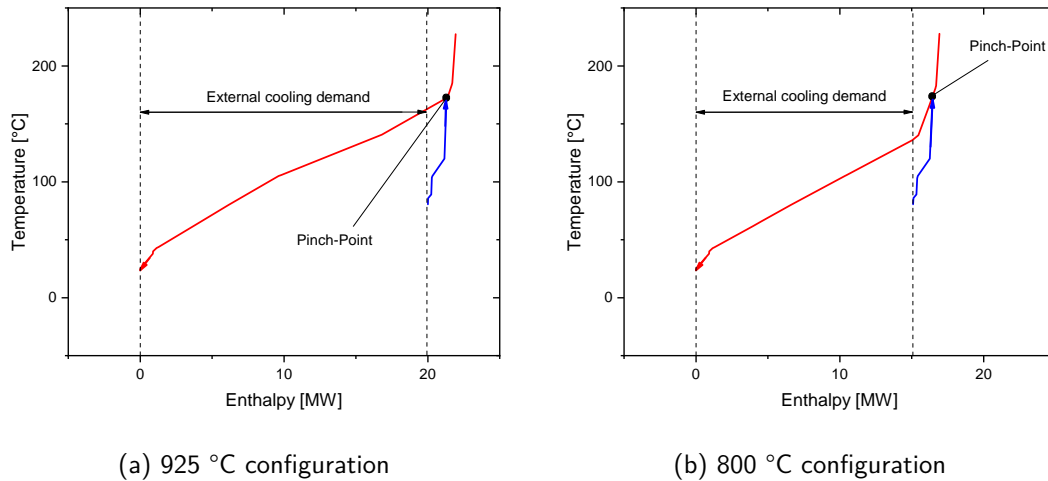


Figure 4.4: Pinch analysis for the complete HyS-cycle

During a pinch analysis, two curves are created in a temperature-enthalpy diagram. One curve summarizes all heater dissipating energy (red curve) and one containing all heaters that require heat input (blue curve). To analyze the heat coupling potential, the blue curve is moved along the x-axis until the two curves only touch in one point. The heat demanding curve must stay under the heat-dissipating curve, to guarantee the heat flux. The touching point of both curves is called the pinch point. Important for this thesis is the yielding external energy demand as indicated in figure 4.4. For both setups, the process needs external cooling. The 925 °C configuration requires 20 MW and the 800 °C configuration requires 15.1 MW. The main reason of the difference between both set-ups is the cooling the liquid after the SAC requires. Figure 3.7 shows the heater block B2 which cools the liquid. For 925 °C B2 requires 7.8 MW of external cooling and for 800 °C it only requires 1.6 MW. Besides heater B2, the heater blocks SHXSEP2 (requires 1.7 MW for both configuration) which cools the gaseous product stream of the SAC and the heater HXAUX2 (925 °C: 2.7 MW, 800 °C: 2.8 MW) as part of the oxygen separation cause the high cooling demand of the flowsheet. The external cooling can be supplied by using lake or river water. Therefore, the total heat demand of the HyS-cycle solely is given by the demand of the SAC section. The demand for electrical energy is determined by summarizing all pumps and compressors of the HyS flowsheet. Additionally the demand of the SDE is taken from del Fabbro Acropinto [18]. Table 4.3 summarizes the total demands of the flowsheet configurations.

Table 4.3: Heat demand of the final HyS configurations

Demand type	925 °C configuration	800 °C configuration
	$[\frac{\text{kJ}}{\text{mol}_{\text{SO}_2}}]$	$[\frac{\text{kJ}}{\text{mol}_{\text{SO}_2}}]$
Cooling demand	(238)	(178)
Bayonet reactor	446	377
Total heat demand	446	377
Pumps & Compressors	15	15
SDE	115	115
Total power demand	130	130

4.2 Techno-economic analysis

This section will discuss the economic effect of the found process modulations. Therefore, the Python script to simulate the thermal particle storage throughout the year was used to compare the five different scenarios summarized in table 3.10. Table 4.4 and table 4.5 list the specific and absolute CAPEX and OPEX costs exemplary for scenario 1a which were calculated as explained in section 2.6.

Table 4.4: Relative and absolute CAPEX for scenario 1a

Category	specific CAPEX [$\frac{\text{€}}{\text{m}^2}$]	absolute CAPEX [Mio. €]	Source
Heliostat	85	43.3	[57]
Tower	68.8	35.1	[41]
Receiver	59.2	30.2	[41]
TES	36.6	18.7	[41]
Bayonet	22.4	11.4	[5]
Kettle boiler	39.3	20.0	[5]
Gas separation	5.5	2.8	[18]
Vacuum system	0.7	0.3	[18]
SDE	29.5	15.0	[5]
EPC	95.0	48.4	[5]
Land	8.8	4.5	[57]
Total	450.7	229.7	

Table 4.5: Relative and absolute OPEX for scenario 1a

Category	specific OPEX [$\frac{\text{€}}{\text{m}^2\text{a}}$]	absolute OPEX [$\frac{\text{Mio. €}}{\text{a}}$]	Source
Variable	7.4	3.8	[62]
Insurance	9.0	4.6	[5]
Maintenance	18.0	9.2	[5]
Employees	3.3	1.7	[63, 64, 14]
Replacement	4.9	2.5	[5]
Total	42.7	21.8	

The CAPEX and OPEX are required to calculate the Levelized costs of hydrogen LCoH. Figure 4.5 exemplary shows the results for scenario 3b.

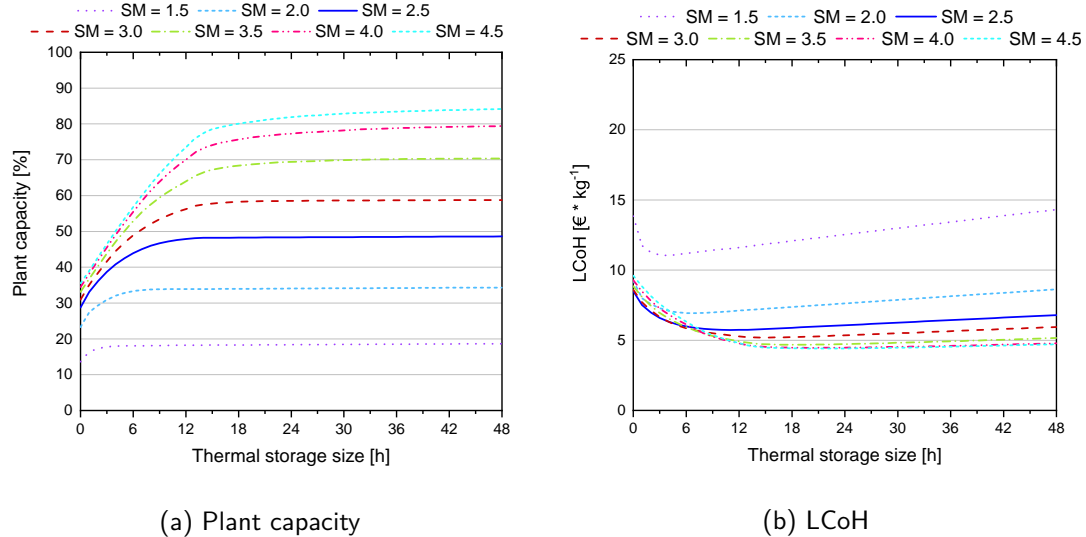


Figure 4.5: Plant capacity and LCoH over storage size for scenario 3b

The left image shows the plant capacity for seven different solar sizes over the varied thermal storage size. It can be seen, that the higher the SM gets, the higher is the possible plant capacity. All curves reach a plateau after a certain thermal storage size, which means a further increase of the thermal storage size does not increase the producible amount of particles. The turning point also moves to higher thermal storage sizes for higher SM because a higher oversizing of the tower systems makes days with worse solar irradiation usable and higher storage sizes can be filled. A third observation is that the plant capacity increase per SM increase shrinks at higher solar multiple. This means, the positive effect of increasing the solar oversizing decreases from step to step. The last observation can be seen for the points of no thermal storage. After an SM of 2.5, the maximum solar utilization is reached. Further increasing the SM does not significantly increase the number of heated particles that can be used in the process without a storage.

The right image of figure 4.5 shows the LCoH as explained in section 2.6. It can be seen, that for every solar size, initially the thermal storage size increase lowers the costs, but at a certain turning point the costs will rise again. The turning point concurs with the turning point of the plant capacity curves because without increasing the plant capacity significantly the larger but more expensive thermal storage does not pay off. The gradient at which the LCoH increases, decreases for higher SM. This is caused by

the smaller fraction of the thermal storage with higher costs for the tower systems. By analyzing all curves at once, a minimum LCoH operating point can be found. As the plant capacity increase slows down for increasing SM, the LCoH curves of higher SM are closer together. At a certain SM, the benefit of increasing the plant capacity will be insufficient. For the shown example of scenario 3b, starting from an SM of 5, the minimum LCoH will increase again. Therefore, this curve is left out in the diagram. Table 4.6 summarizes the minimum LCoH operating points for all five scenarios.

Table 4.6: Best operating points (lowest LCoH) for all scenarios

Scenario	Thermal storage size [h]	SM [-]	Tower number [-]	Plant capacity [%]	LCoH [$\frac{\text{€}}{\text{kg}}$]
1a	19	4.6	15	81.6	6.09
1b	21	4.6	13	82.4	5.54
2	18	4.0	23	75.2	5.73
3a	19	4.5	47	80.1	4.96
3b	22	4.5	41	81.4	4.42

The values of the storage size and the SM seem to vary a lot, but as the small slopes of the lowest LCoH values indicate, varying these values does not significantly influence the LCoH. For example, the results of scenario 2 stand out as they are optimal at a lower SM than the other scenarios. But the LCoH difference between the lowest value of SM 4.0 and SM 4.5 is just $0.009 \frac{\text{€}}{\text{kg}}$. Therefore, varying these values slightly to fit certain construction demands will not significantly influence the economically performance. More meaningful is the comparison of the scenarios among each other. The first thing to observe here is the positive influence of the 800 °C Bayonet configuration. For example, scenario 1b is $0.55 \frac{\text{€}}{\text{kg}}$ cheaper than scenario 1a. This is caused by the lower specific heat demand of that configuration, resulting in smaller demand of tower systems as the tower numbers indicate. The second effect to observe is the benefit of scale. By comparing scenarios with the same Bayonet configuration (e.g. 1b and 3b), the scenarios with a higher production scale deliver cheaper LCoH. A larger production scale lowers the specific costs of system components such as the bayonet reactor, the kettle boiler or the SDE and therefore decreases the LCoH. To better understand the

influence of different system parts, figure 4.6 shows the composition of the CAPEX for scenario 1b.

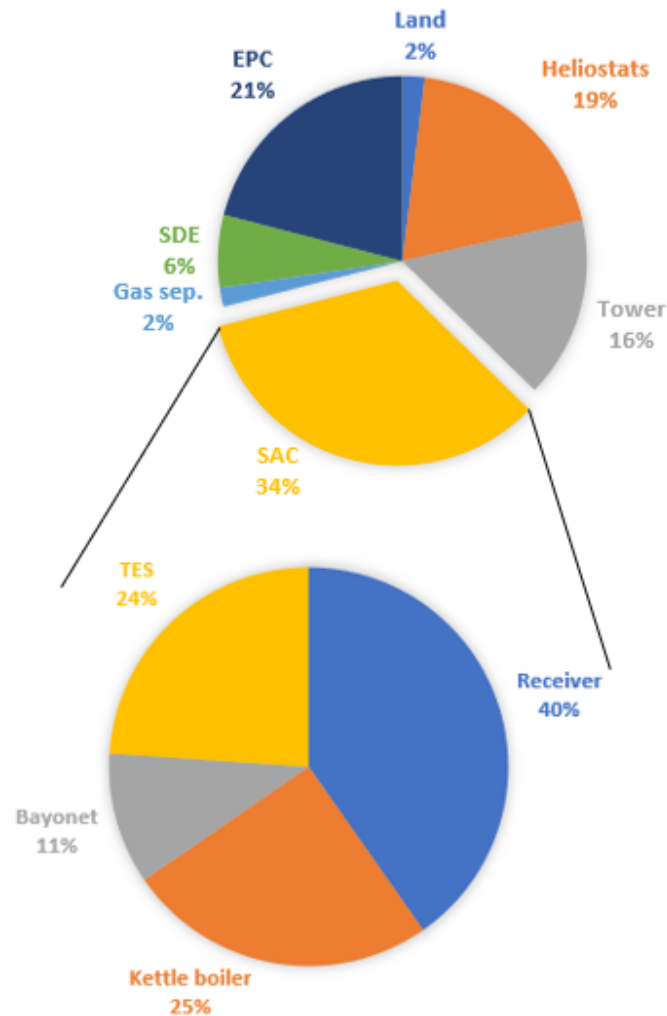


Figure 4.6: CAPEX composition of scenario 1b

The EPC costs were set to be 33 % of the CAPEX, excluding the receiver costs as they already include indirect costs [37]. This decreases the fraction of the EPC to a total 21 %. The biggest share of the investment costs have the heliostats and the solar tower with a combined 35 %. All components important for the SAC section make up 34 %. How this influences the LCoH is shown in figure 4.7 for the scenarios 1b and 3b.

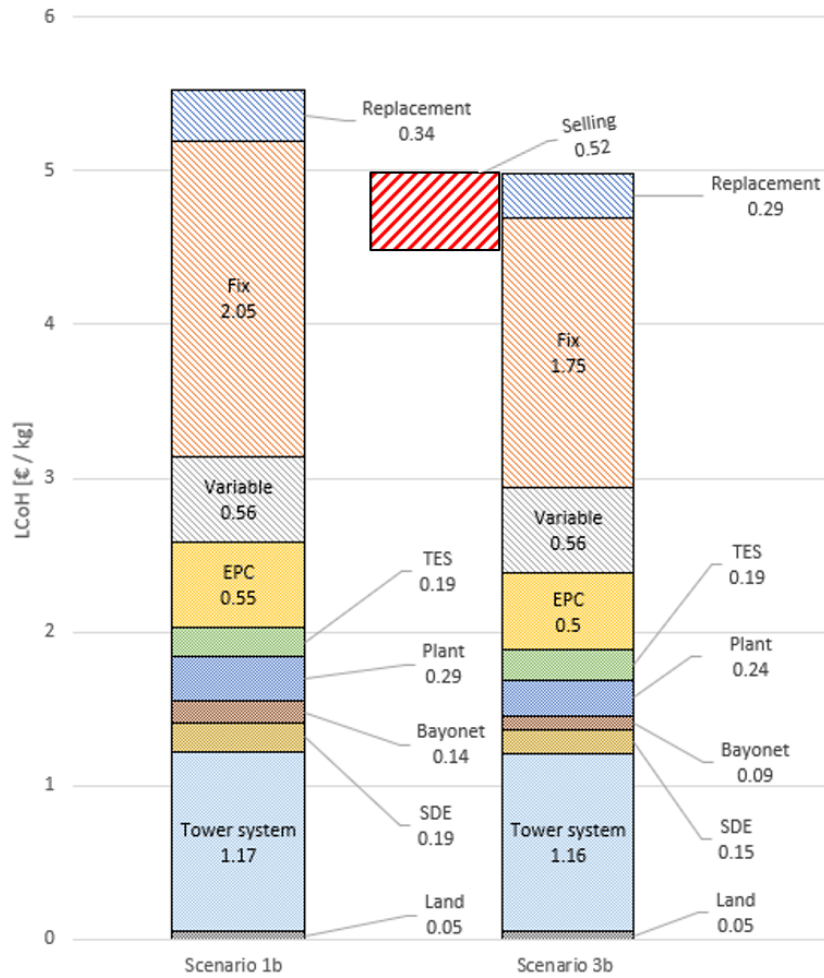
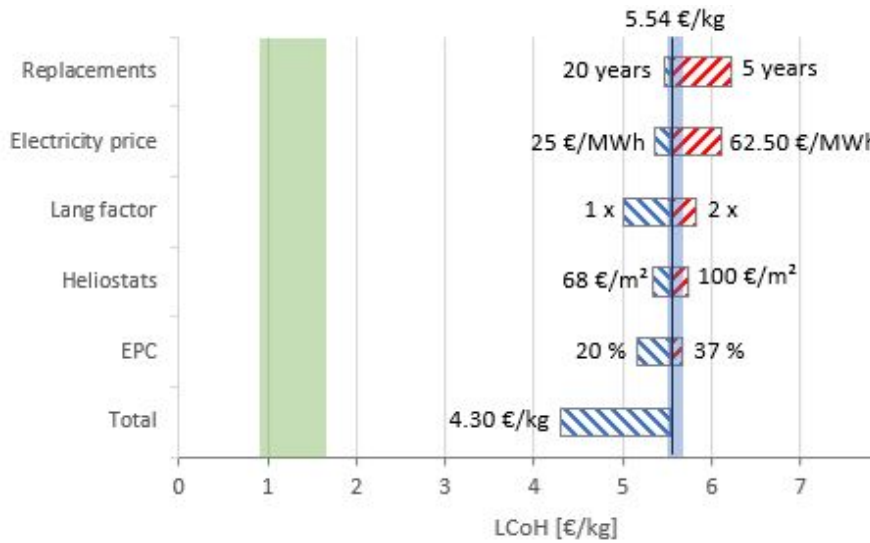


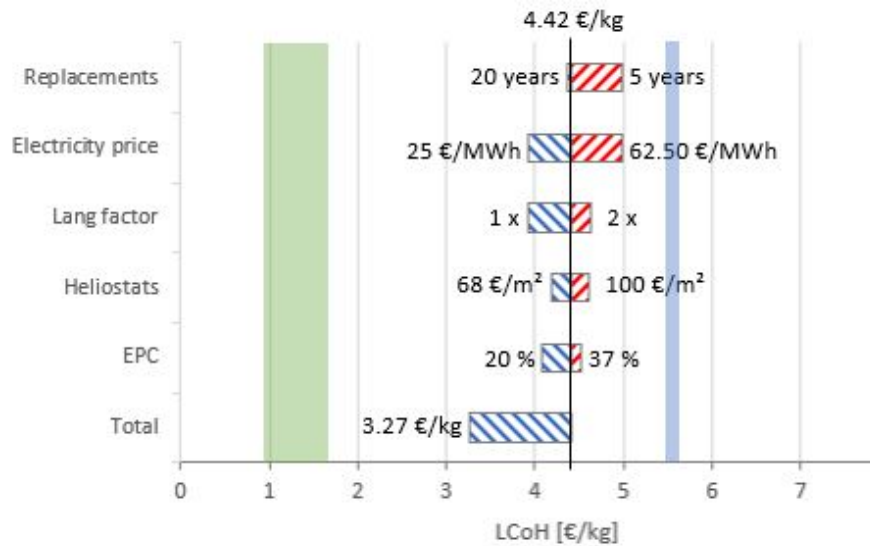
Figure 4.7: Composition of LCoH for scenario 1b and 3b

The comparison of the LCoH composition for the two 800 °C scenarios is important to understand the main cost influences. The figure shows the absolute fraction each system part has on the LCoH. The OPEX are symbolized by a striped filling, the CAPEX are symbolized by a dotted filling. For scenario 1b the fraction of the OPEX on the LCoH is larger than the fraction of the CAPEX, which indicates the influence of operational costs like electricity or working force. The scenarios 3a and 3b produce more hydrogen than the copper production requires. Therefore the overproduced hydrogen can be sold at the price named in table 3.12. The fraction the LCoH gets reduced by the selling is shown by the red striped box on the left of the scenario 3b bar. Between the two scenarios, the influence of scale is shown. All component related costs and the replacement of them is cheaper for the larger scale of scenario 3b. The variable costs

consisting of the electricity costs stay the same as they are directly coupled to the produced mass. As the component related costs (mostly CAPEX) increase for smaller scales, the costs depending on the CAPEX (EPC and fix OPEX) will increase too. As the fix OPEX costs are paid every year for the observed operation time, the increase of the fix OPEX costs is larger than for the EPC. To decrease the LCoH one could try to find cheaper tower systems. As figure 4.7 shows, even when the tower systems would not cost anything, the minimum LCoH reachable is $4.37 \frac{\text{€}}{\text{kg}}$ for scenario 1b and $3.26 \frac{\text{€}}{\text{kg}}$ for scenario 3b. To further analyze the potentials, a sensitivity analysis was performed. Figure 4.8 shows the results for the both scenarios.



(a) Scenario 1b



(b) Scenario 3b

Figure 4.8: Tornado diagrams of sensitivity analysis, green highlighted: conventionally produced hydrogen, blue highlighted: hydrogen produced by standard electrolysis (plant capacity = 85 %)

For the sensitivity analysis the replacement intervals, the electricity price, the Lang-factors, the heliostat costs and the EPC share were investigated. The replacement interval of 10 years was halved and doubled to see the influence. It is noticeable, that the interval of 5 years increases the LCoH more than the interval of 20 years would decrease the costs. The electricity price was changed to 25 $\frac{\text{€}}{\text{MWh}}$ which represents the electricity price in Australia without a carbon dioxide tax (appr. 40 $\frac{\text{AUD}}{\text{MWh}}$) and up to 62.5 $\frac{\text{€}}{\text{MWh}}$ which represents the electricity price in Australia for the required carbon

dioxide tax in 2035 (appr. $100 \frac{\text{AUD}}{\text{MWh}}$) [62]. The electricity price shows a high potential to influence the LCoH and should be part of improvement considerations. The Lang-factors, as selected in section 3.2, were decreased to 1 for representing a well-known technology. The increase to 2 was performed to show the influence of the Lang-factor. Similar to the electricity price, the Lang-factors influence the LCoH strongly. In future scenarios, the technology might not be novel and lower Lang-factors are possible. Furthermore, different heliostat costs are investigated. As Rosenstiel mentioned, the BrightSource heliostat costs could decrease to $68 \frac{\text{€}}{\text{m}^2}$ ($80 \frac{\text{USD}}{\text{m}^2}$) [57]. As this price is possible for future scenarios, it is considered in this sensitivity analysis. The EPC factor was decreased to 20 % to represent a more known process build-up like a concentrated solar power plant and increased to 37 % to represent the maximum value for CSTE systems. The influence of a lower EPC factor is even larger than the cheaper heliostat costs. Subsequently, all positive effects were chosen to calculate the total LCoH value at the bottom. This price represents a value possible for a futuristic scenario. The green marked area represents the price range for conventionally produced hydrogen from fossil fuels [61] and the blue marked area represents the price of hydrogen from conventional water electrolysis fed by electricity from the grid with a plant capacity of 85 % [66].

It can be seen, that the solar concentrated HyS-cycle can generate cheaper hydrogen than the standard electrolysis procedure. But even the cheapest scenario with all positive sensitivity assumptions is not able to reach the price range of conventionally produced hydrogen. To justify the higher costs on the market, the green hydrogen entitlement can be used. But as the electricity used for the SDE comes from the grid and the additional particle heater would burn fossil fuels, the hydrogen produced in the set-up of this thesis is more environmentally friendly than conventional hydrogen but not completely green hydrogen. With the increase of renewable energy in the grid, this share would also increase. Since the HyS-cycle replaces a part of the electricity demand of conventional electrolysis with a heat demand, the footprint of the product will always be lower than grid-based hydrogen from electrolysis.

5 Conclusion and Outlook

A detailed model of the particle-heated Bayonet reactor was created using Aspen Plus and Python. The different model parts were validated separately. At first a kinetic for the SO_3 decomposition was found and validated. The tested Bayonet configuration indicated that equilibrium conversions are possible and therefore no kinetic equations were required in the final set-up. Subsequently, the heat transfer calculations were tested by reproducing existing simulation results from a particle-heated tube reactor [42] and an air-heated Bayonet reactor [43]. After validating the Bayonet model a parameter study pointed out improvement possibilities. Based on the improvement opportunities, two final Bayonet configurations were introduced. Both set-ups assume ceramic foam packings to increase the inner heat transfer and an increased particle inlet temperature of 1,100 °C. The set-ups differ in the chosen catalytic inlet temperature. The first model uses 925 °C, as this temperature is required to stabilize the iron oxide catalyst at 15 bar reactor pressure. The second model follows an assumption of Guerra Niehoff, who considered future catalysts could be able to stay stable at lower temperatures of 800 °C [5]. The last optimization step of both models was to increase the sulfuric acid mass flowrate until the upper limit of the reactor length is reached. The upper limit was chosen to be 10 m, as this size is the maximum that is producible for the chosen geometry defined by Binder [43].

Both reactor models were implemented in an existing HyS flowsheet in Aspen Plus. As iterative procedures were used to set up the reactor integration, the flowsheets have deviations to the required points, such as the mass balance of the SAC and the inlet sulfuric acid concentration. Since the deviations are smaller than 0.2 %, they are assumed to be negligible. Following the reactor implementation, the product purification methods were adapted to the requirements of the consumer - a copper production in Australia. After all flowsheet adjustments, a pinch-analysis for both Bayonet configurations was performed. Both flowsheet configurations, without considering the heat demand of the reactor itself, only had a cooling demand. The 925 °C flowsheet needed 20 MW external cooling capacity and the 800 °C flowsheet needed 15.1 MW. The

cooling demand is considered to be satisfied by lake or river water and was not observed further.

To simulate the CSTE system, the heliostat field was designed in the first place. Therefore, heliostats from the company BrightSource Energy and an optimized design of a 20 MW configuration of the CentRec from Frantz were used [37]. The heliostat field was designed for clear sky conditions, but to observe realistic behaviors, a Python script was created. The script calculates the solar altitude and uses real DNI values from the year 2005, both for the location of Olympic Dam in an hourly resolution. The script will calculate the efficiency of the field and the receiver for every time point and can therefore calculate the resulting tower system performance. In this way, it was possible to simulate the thermal storage in an hourly resolution and to estimate the plant capacity of the solar integration. It was assumed, that the HyS plant will be shut down for 32 coherent days which were picked by the Python script to be the lowest irradiated days. Thereby, resulting a total production time of $7,992 \frac{\text{h}}{\text{a}}$. Furthermore, it was assumed that the particle demand which can not be satisfied by the solar integration is fulfilled by additional burners. The particle demand of the HyS plant was obtained for both Bayonet configurations using the previously created flowsheets.

With the possibility to calculate the plant capacity, a techno-economic analysis could be performed. Therefore, the investment costs for all involved components were calculated. Estimations for the operational costs were made and adapted to the Australian site. The TEA looked at different scenarios for different production scales of the HyS plant. The goals of the scenarios were to satisfy either the fuel or the oxygen demand of the copper production for either the current or the announced scale of the copper production. Additionally, the different Bayonet configurations were considered. The LCoH was calculated for all five scenarios considering different solar multiple and thermal storage sizes. The best configuration resulting from the lowest LCoH was determined for all scenarios. Hereby, the largest scenario with a required HyS production rate of $81 \frac{\text{t}_{\text{H}_2}}{\text{d}}$ yielded the lowest LCoH of $4.42 \frac{\text{€}}{\text{kg}}$. To estimate potential improvements, a sensitivity analysis was performed. By considering all positive improvements an LCoH of $3.27 \frac{\text{€}}{\text{kg}}$ is assumed to be possible.

The presented results of this thesis show potentials for the solar-heated HyS-cycle. The found LCoH are subject to assumptions about possibilities that future technology could enable. Without the possibility to produce heating particles at temperatures of $1,100 \text{ °C}$ or to use catalysts that are stable at lower temperatures despite the high reactor pressure, the calculated price range for hydrogen is not reachable. Nonetheless, a higher hydrogen price compared to conventional production is justifiable with the

efforts of producing hydrogen with lower carbon dioxide emissions. Alternatives, that produce green hydrogen like PV-powered water electrolysis are more expensive than the HyS-cycle developed in this thesis. The advantage of the HyS-cycle in comparison to a grid-powered water electrolysis is the lower energy consumption and thereby the lower carbon dioxide footprint.

The created Bayonet model in this thesis uses multiple simplifications. As currently no experimental data for a particle-heated Bayonet reactor at 15 bar using an iron oxide catalyst exists, the exact validation of the created model was not possible. For future considerations, the addition of a pressure drop calculation or a more precise discretization of the model, especially in the vaporization section, could enable more accurate results.

The efficiency of the tower system was calculated to be relatively low. Therefore, changes in the tower system design could help to improve the total plant performance. One possibility to improve the field efficiency of the heliostats is to use a surround field design by placing heliostats behind the tower. This possibility was already discussed for the CentRec by Frantz et al. [37] and is made possible by using a high tower and tilting the receiver.

Interesting for further considerations is a more detailed cost analysis of the benefits occurring from the cooperation of the HyS plant with the copper production. The copper production requires an air separation unit to produce the required oxygen. This air separation unit would not be needed anymore and therefore the costs of the copper production can be lowered. Additionally, the copper production uses sulfuric acid to extract uranium from the mined ore. The sulfuric acid is produced from the sulfur dioxide in the off-gas of the flash furnace using an acid plant. Hereby, existing infrastructure can be used or even replaced, as the HyS-cycle uses both chemicals as well. Thereby production cost decreases are expected.

List of Abbreviations

List of Abbreviations

CO_2	Carbon dioxide
$\text{Fe}_2(\text{SO}_4)_3$	Iron(III) sulfate
Fe_2SO_3	Iron(III) oxide
HSO_3^-	Hydrogen sulfite
HSO_4^-	Hydrogen sulfate
H_2O	Water
H_2SO_4	Sulfuric acid
$\text{H}_2\text{S}_2\text{O}_7$	Disulfuric acid
H_3O^+	Hydronium
SO_2	Sulfur dioxide
SO_3	Sulfur trioxide
SO_4^{2-}	Sulfate
ANF	Annuity factor
CAPEX	Capital expenses
CSTE	Concentrated solar thermal energy
DLR	The German Aerospace Center
DNI	Direct normal irradiance

DOE	Department of Energy
eNRTL	Electrolyte Non-Random Two-Liquid
EPC	Engineering and Procurement costs
HFLCAL	Heliostat field layout calculations
HyS	Hybrid Sulfur (cycle or process)
IPCC	Intergovernmental Panel on Climate Change
LCoH	Levelized costs of hydrogen
LHV	Lower heating value
LPG	Liquefied petroleum gas
OPEX	Operational expenses
PEM	Proton exchange membrane
s-PBI	Sulfonated polybenzimidazole
SAC	Sulfuric acid cracking
SDE	Sulfur-Dioxide-Depolarised Electrolysis
SI	Sulfur iodine
SiC	Silicon carbide
SM	Solar multiple
SNL	Sandia National Laboratory
SV	Space velocity
TES	Thermal energy storage
VDI	Association of German Engineers
WHSV	Weight hourly space velocity

List of Indexes

0	Standard
---	----------

1	Point 1
2	Point 2
A,sp	Area-specific
ann	Annular duct
ap	Aperture
aq	Aqueous
cav	Cavity
CS	Counter stream
f	Fluid
g	Gaseous
gas	Interstitial gas
i	Inner
is	Insulation
l	Liquid
lam,2300	Laminar state
MS	Main stream
o	Outer
pack	Packed reactor section
par	Particle
PS	Particle stream
R	Reaction
rad	Radiation
rec	Receiver
SO	First layer to inner bulk

st	Storage
tow	Tower
tr	Transport system
tur,10000	Turbulent state
W	Wall
WP	Wall to particle
WS	Wall to first layer

List of Symbols

α	Heat transfer coefficient	$\left[\frac{\text{W}}{\text{m}^2\text{K}}\right]$
β	Absorptivity	[-]
ΔH	Enthalpy change	[J]
δ	Surface roughness	[m]
\dot{m}	Mass flow	$\left[\frac{\text{kg}}{\text{s}}\right]$
\dot{n}	Molar flow	$\left[\frac{\text{mol}}{\text{s}}\right]$
\dot{Q}	Heat flow	[W]
ϵ	Emissivity	[-]
η	Efficiency	[-]
η_{vis}	Dynamic viscosity	$\left[\frac{\text{N}\cdot\text{s}}{\text{m}^2}\right]$
γ	Intermittency factor	[-]
λ	Thermal conductivity	$\left[\frac{\text{W}}{\text{m}\cdot\text{K}}\right]$
μ	Chemical potential	$\left[\frac{\text{J}}{\text{kg}}\right]$
ν	Stoichiometric coefficient	[-]
ν_{vis}	Kinematic viscosity	$\left[\frac{\text{m}^2}{\text{s}}\right]$
ρ	Density	$\left[\frac{\text{kg}}{\text{m}^3}\right]$

σ_r	Stefan-Boltzmann constant	$\left[\frac{\text{W}}{\text{m}^2\text{K}^4}\right]$
ε	Porosity	[-]
φ	Surface coverage factor	[-]
ξ	Friction factor	[-]
A	Area	$[\text{m}^2]$
a	Affinity	$\left[\frac{\text{J}}{\text{kg}}\right]$
b	Diameter ratio	[-]
C	Costs	[€]
c	Concentration	$\left[\frac{\text{mol}}{\text{m}^3}\right]$
c_p	Specific heat capacity at constant pressure	$\left[\frac{\text{J}}{\text{kg K}}\right]$
$C_{W,\text{bulk}}$	Radiation coefficient	$\left[\frac{\text{W}}{\text{m}^2\text{K}^4}\right]$
d, D	Diameter	[m]
d_{hyd}	Hydraulic diameter	[m]
E_A	Activation energy	[J]
f_{EPC}	EPC factor	[%]
f_L	Lang factor	[-]
H	Height	[m]
h	Heat loss coefficient	$\left[\frac{\text{W}}{\text{m}^2\text{K}}\right]$
j	Interest rate	[%]
k	Reaction speed constant	$\left[\frac{\text{mol}}{\text{s}}\right]$
K_{fix}	Fix operational costs	[€]
K_{rep}	Replacement costs	[€]
K_{var}	Variable operational costs	[€]
L	Length	[m]

L_c	Characteristic Length	[m]
M	Molar mass	$[\frac{\text{kg}}{\text{mol}}]$
n	Operation time	[a]
Nu	Nusselt number	[-]
P	Power	[W]
Pr	Prandtl number	[-]
R	Ideal gas coefficient	$[\frac{\text{J}}{\text{mol K}}]$
r	Radius	[m]
Re	Reynolds number	[-]
T	Temperature	[K]
t_c	Residence contact time	[s]
U	Transmittance	$[\frac{\text{W}}{\text{m}^2\text{K}}]$
V	Volume	$[\text{m}^3]$
v	Velocity	$[\frac{\text{m}}{\text{s}}]$
z	Reaction conversion	[-]

Bibliography

- [1] Abe, J. O., Popoola, A., Ajenifuja, E., and Popoola, O. M. "Hydrogen energy, economy and storage: Review and recommendation". In: *International Journal of Hydrogen Energy* 44.29 (2019), pages 15072–15086. ISSN: 03603199. DOI: 10.1016/j.ijhydene.2019.04.068.
- [2] Climate Change, I. P. on. *Global warming of 1.5° C: an IPCC special report on the impacts of global warming of 1.5° C above pre-industrial levels and related global greenhouse gas emission pathways, in the context of strengthening the global response to the threat of climate change, sustainable development, and efforts to eradicate poverty*. Intergovernmental Panel on Climate Change, 2018.
- [3] Roeb, M., Brendelberger, S., Rosenstiel, A., Agrafiotis, C., Monnerie, N., Budama, V., and Jacobs, N. *Wasserstoff als ein Fundament der Energiewende Teil 1: Technologien und Perspektiven für eine nachhaltige und ökonomische Wasserstoffversorgung*. Edited by Deutsches Zentrum für Luft- und Raumfahrt e. V. 2005.
- [4] Umweltbundesamt. *Erneuerbare Energien in Deutschland: Daten zur Entwicklung im Jahr 2020*. 2021.
- [5] Guerra Niehoff, A. "Technische Analyse und wirtschaftliche Bewertung von Solarreaktoren zur Schwefelsäurespaltung für die thermochemische Erzeugung von Wasserstoff". PhD thesis. RWTH Aachen University, 2020.
- [6] Brown, L. C., Besenbruch, G. E., Lentsch, R. D., Schultz, K. R., Funk, J. F., Pickard, P., Marshall, A. C., and Showalter, S. K. *HIGH EFFICIENCY GENERATION OF HYDROGEN FUELS USING NUCLEAR POWER*. Report. 2003.
- [7] Corgnale, C., Gorenssek, M. B., and Summers, W. A. "Review of Sulfuric Acid Decomposition Processes for Sulfur-Based Thermochemical Hydrogen Production Cycles". In: *Processes* 8.11 (2020), page 1383. DOI: 10.3390/pr8111383.

- [8] Onuki, K., Kubo, S., Terada, A., Sakaba, N., and Hino, R. "Thermochemical water-splitting cycle using iodine and sulfur". In: *Energy & Environmental Science* 2.5 (2009), page 491. ISSN: 1754-5692. DOI: 10.1039/b821113m.
- [9] Gorenssek, M. B. and Summers, W. A. "Hybrid sulfur flowsheets using PEM electrolysis and a bayonet decomposition reactor". In: *International Journal of Hydrogen Energy* 34.9 (2009), pages 4097–4114. ISSN: 03603199. DOI: 10.1016/j.ijhydene.2008.06.049.
- [10] Gorenssek, M. B. and Edwards, T. B. "Energy Efficiency Limits for a Recuperative Bayonet Sulfuric Acid Decomposition Reactor for Sulfur Cycle Thermochemical Hydrogen Production". In: *Industrial & Engineering Chemistry Research* 48.15 (2009), pages 7232–7245. ISSN: 0888-5885. DOI: 10.1021/ie900310r.
- [11] Garrick, T. R., Gullledge, A., Staser, J. A., Benicewicz, B., and Weidner, J. W. "Polybenzimidazole Membranes for Hydrogen Production in the Hybrid Sulfur Electrolyzer". In: *ECS Transactions* 66.3 (2015), pages 31–40. ISSN: 1938-6737. DOI: 10.1149/06603.0031ecst.
- [12] Gorenssek, M. B., Corgnale, C., and Summers, W. A. "Development of the hybrid sulfur cycle for use with concentrated solar heat. I. Conceptual design". In: *International Journal of Hydrogen Energy* 42.33 (2017), pages 20939–20954. ISSN: 03603199. DOI: 10.1016/j.ijhydene.2017.06.241.
- [13] European-central-bank. https://www.ecb.europa.eu/stats/policy_and_exchange_rates/euro_reference_exchange_rates/html/eurofxref-graph-usd.en.html. 2021.
- [14] The World bank group. *Inflation, consumer prices (annual %)*. 2021.
- [15] Corgnale, C. and Summers, W. A. "Solar hydrogen production by the Hybrid Sulfur process". In: *International Journal of Hydrogen Energy* 36.18 (2011), pages 11604–11619. ISSN: 03603199. DOI: 10.1016/j.ijhydene.2011.05.173.
- [16] Hinkley, J. T., O'Brien, J. A., Fell, C. J., and Lindquist, S.-E. "Prospects for solar only operation of the hybrid sulphur cycle for hydrogen production". In: *International Journal of Hydrogen Energy* 36.18 (2011), pages 11596–11603. ISSN: 03603199. DOI: 10.1016/j.ijhydene.2011.06.048.
- [17] Kromer, M., Roth, K., Takata, R., and Chin, P. *Support for Cost Analyses on Solar-Driven High Temperature Thermochemical Water-Splitting Cycles*. Report. 2011.

- [18] Del Fabbro Arcopinto, G. L. "TECHNO ECONOMIC ANALYSIS OF THE HYBRID SULFUR CYCLE FOR THE PRODUCTION OF HYDROGEN THROUGH SOLAR SOURCE". Master's thesis. 2021.
- [19] Noglik, A., Roeb, M., Sattler, C., and Pitz-Paal, R. "Experimental study on sulfur trioxide decomposition in a volumetric solar receiver-reactor". In: *International Journal of Energy Research* 33.9 (2009), pages 799–812. ISSN: 0363907X. DOI: 10.1002/er.1514.
- [20] Thomey, D., Oliveira, L. de, Säck, J.-P., Roeb, M., and Sattler, C. "Development and test of a solar reactor for decomposition of sulphuric acid in thermochemical hydrogen production". In: *International Journal of Hydrogen Energy* 37.21 (2012), pages 16615–16622. ISSN: 03603199. DOI: 10.1016/j.ijhydene.2012.02.136.
- [21] Agrafiotis, C., Thomey, D., Oliveira, L. de, Overbeck, N., Thanda, V. K., Roeb, M., and Sattler, C. "Solar energy conversion and storage through sulphur-based thermochemical cycles implemented on centrifugal particle receivers". In: *SOLARPACES 2019: International Conference on Concentrating Solar Power and Chemical Energy Systems*. AIP Conference Proceedings. AIP Publishing, 2020, page 170001. DOI: 10.1063/5.0028766.
- [22] Moore, R., Pickard, P., Parma, E., Vernon, M., Gelbard, F., and Leard, R. "INTEGRATED BOILER, SUPERHEATER, AND DECOMPOSER FOR SULFURIC ACID DECOMPOSITION". US 7,645,437 B1. 2010.
- [23] Russ, B. *Sulfur Iodine Process Summary For the Hydrogen Technology Down-Selection*. Report. 2009.
- [24] *VDI Heat Atlas*. Berlin, Heidelberg: Springer Berlin Heidelberg, 2010. ISBN: 978-3-540-77876-9. DOI: 10.1007/978-3-540-77877-6.
- [25] Thanda, V. K. "Thermochemical Production of Sulfur as Solar fuel: Design and development of moving bed heat exchanger for sulfuric acid evaporation heated by ceramic particles". Master's thesis. Universität Duisburg Essen, 2018.
- [26] Niessch, J., Köneke, D., and Weinspach, P.-M. "Heat transfer and flow of bulk solids in a moving bed". In: *Chemical Engineering and Processing: Process Intensification* 33.2 (1994), pages 73–89. ISSN: 02552701. DOI: 10.1016/0255-2701(94)85006-2.
- [27] Baehr, H. D. and Kabelac, S. *Thermodynamik*. Berlin, Heidelberg: Springer Berlin Heidelberg, 2016. ISBN: 978-3-662-49567-4.

- [28] Ishikawa, H., Ishii, E., Uehara, I., and Nakane, M. "CATALYZED THERMAL DECOMPOSITION OF H₂SO₄ AND PRODUCTION OF HBr BY THE REACTION OF SO₂ WITH Br₂ AND H₂O". In: *Int. J. Hydrogen Energy* 7.3 (1982), pages 237–246.
- [29] Kondamudi, K. and Upadhyayula, S. "Kinetic studies of sulfuric acid decomposition over Al–Fe₂O₃ catalyst in the sulfur-iodine cycle for hydrogen production". In: *International Journal of Hydrogen Energy* 37.4 (2012), pages 3586–3594. ISSN: 03603199. DOI: 10.1016/j.ijhydene.2011.05.026.
- [30] Noglik, A., Roeb, M., Rzepczyk, T., Hinkley, J., Sattler, C., and Pitz-Paal, R. "Solar Thermochemical Generation of Hydrogen: Development of a Receiver Reactor for the Decomposition of Sulfuric Acid". In: *Journal of Solar Energy Engineering* 131.1 (2009). ISSN: 0199-6231. DOI: 10.1115/1.3027505.
- [31] van der Merwe, A. F. "Reaction kinetics of the iron-catalysed decomposition of SO₃". Master's thesis. 2014.
- [32] Ginosar, D. M., Rollins, H. W., Petkovic, L. M., Burch, K. C., and Rush, M. J. "High-temperature sulfuric acid decomposition over complex metal oxide catalysts". In: *International Journal of Hydrogen Energy* 34.9 (2009), pages 4065–4073. ISSN: 03603199. DOI: 10.1016/j.ijhydene.2008.09.064.
- [33] Banerjee, A. M., Shirole, A. R., Pai, M. R., Tripathi, A. K., Bharadwaj, S. R., Das, D., and Sinha, P. K. "Catalytic activities of Fe₂O₃ and chromium doped Fe₂O₃ for sulfuric acid decomposition reaction in an integrated boiler, preheater, and catalytic decomposer". In: *Applied Catalysis B: Environmental* 127 (2012), pages 36–46. ISSN: 09263373. DOI: 10.1016/j.apcatb.2012.07.030.
- [34] Giaconia, A., Sau, S., Felici, C., Tarquini, P., Karagiannakis, G., Pagkoura, C., Agrafiotis, C., Konstandopoulos, A. G., Thomey, D., Oliveira, L. de, Roeb, M., and Sattler, C. "Hydrogen production via sulfur-based thermochemical cycles: Part 2: Performance evaluation of Fe₂O₃-based catalysts for the sulfuric acid decomposition step". In: *International Journal of Hydrogen Energy* 36.11 (2011), pages 6496–6509. ISSN: 03603199. DOI: 10.1016/j.ijhydene.2011.02.137.
- [35] Buck, R. and Schwarzbözl, P. "4.17 Solar Tower Systems". In: *Comprehensive Energy Systems*. Elsevier, 2018, pages 692–732. ISBN: 9780128149256. DOI: 10.1016/B978-0-12-809597-3.00428-4.
- [36] Bayer Botero, N. "Technisch-wirtschaftliche Bewertung des hybriden Schwefelsäurekreisprozesses zur solaren Produktion von Wasserstoff". PhD thesis. RWTH Aachen University, 2014.

- [37] Frantz, C., Buck, R., and Amsbeck, L. "DESIGN AND COST STUDY OF IMPROVED SCALED-UP CENTRIFUGAL PARTICLE RECEIVER BASED ON SIMULATION". In: *14th International Conference on Energy Sustainability* (2020).
- [38] Gobereit, B. *PEGASUS - WP2*. Presentation. 2017.
- [39] Ulrich, G. and Vasudevan, P. *CHEMICAL ENGINEERING - PROCESS DESIGN AND ECONOMICS A PRACTICAL GUIDE*. 2004.
- [40] Falcone, P. "A handbook for solar central receiver design". In: (1986). DOI: 10.2172/6545992.
- [41] Frantz, C., Ebert, M., Amsbeck, L., and Buck, R. *Design and cost study of improved scaled-up receiver version based on simulation results*. Report. 2019.
- [42] Belina, J. J. "Thermochemical sulphur cycle for long-term storage of concentrated solar thermal energy: Process implementation of a particle heated reactor concept and techno-economic optimization". Master's thesis. RWTH Aachen University, 2021.
- [43] Binder, F. "Thermodynamische Modellierung und Dimensionierung eines luftbeheizten Reaktors mit integrierter Wärmerückgewinnung zur Schwefelsäurespaltung". Master's thesis. TH Köln, 2017.
- [44] Corgnale, C., Ma, Z., and Shimpalee, S. "Modeling of a direct solar receiver reactor for decomposition of sulfuric acid in thermochemical hydrogen production cycles". In: *International Journal of Hydrogen Energy* 44.50 (2019), pages 27237–27247. ISSN: 03603199. DOI: 10.1016/j.ijhydene.2019.08.231.
- [45] Mathias, P. M. *MODELING THE SULFUR-IODINE CYCLE Aspen Plus Building Blocks and Simulation Models*. Report. 2002.
- [46] Kaur, H., Wang, M., Gorenssek, M. B., and Chen, C.-C. *Thermodynamic modeling of the hybrid sulfur (HyS) cycle for hydrogen production*. 2018.
- [47] Corgnale, C., Shimpalee, S., Gorenssek, M., Weidner, J. W., and Summers, W. "Modeling of a Bayonet Reactor for Sulfuric Acid Decomposition in Thermo-Electrochemical Sulfur Based Hydrogen Production Processes". In: *ECS Transactions* 75.43 (2017), pages 7–15. ISSN: 1938-6737. DOI: 10.1149/07543.0007ecst.
- [48] Connolly, S. M., Zabolotny, E., McLaughlin, D. F., and Lahoda, E. J. "Design of a composite sulfuric acid decomposition reactor, concentrator, and preheater for hydrogen generation processes". In: *International Journal of Hydrogen Energy* 34.9 (2009), pages 4074–4087. ISSN: 03603199. DOI: 10.1016/j.ijhydene.2008.07.126.

- [49] BHP Group. "Chapter 2 - Existing Operation". In: *Olympic Dam Expansion Draft Environmental Impact Statement 2009*. Edited by BHP Group. Volume Chapter 2. 2009.
- [50] Schlesinger, M. E. and Biswas, A. K. *Extractive metallurgy of copper*. 5th ed. Amsterdam and Boston: Elsevier, 2011. ISBN: 9780080967899.
- [51] BHP Group. "Chapter 5 - Description of the proposed expansion". In: *Olympic Dam Expansion Draft Environmental Impact Statement 2009*. Edited by BHP Group. Volume Chapter 5. 2009.
- [52] Indaily.com. <https://indaily.com.au/news/2020/10/20/bhp-scrap-major-olympic-dam-expansion/>, 27.09.2021. 2020.
- [53] Agert, C., Brand, U., Deniz, Ö., and Dyck, A. *Wasserstoff als ein Fundament der Energiewende Teil 2: Sektorenkopplung und Wasserstoff: Zwei Seiten der gleichen Medaille*. Edited by Deutsches Zentrum für Luft- und Raumfahrt e. V. 2020.
- [54] White, M., Haywood, R., Taylor, W., Chen, S., Ranasinghe, J., and West, R. *Improved Copper Flash Smelting at Olympic Dam*. Conference paper. 2015.
- [55] BHP Group. "Chapter 22 - Health and Safety". In: *Olympic Dam Expansion Draft Environmental Impact Statement 2009*. Edited by BHP Group. 2009.
- [56] Augsburg, G. "Thermo-economic optimisation of large solar tower power plants". PhD thesis. 2013. DOI: 10.5075/epfl-thesis-5648.
- [57] Rosenstiel, A. "Techno-economic study of a concentrated solar thermal plant with sulphur as thermo-chemical energy storage for baseload power generation and sulphuric acid recycling". Master's thesis. Technische Universität Berlin, 2018.
- [58] Michalsky, J. J. "The Astronomical Almanac's algorithm for approximate solar position (1950–2050)". In: *Solar Energy* 40.3 (1988), pages 227–235. ISSN: 0038092X. DOI: 10.1016/0038-092X(88)90045-X.
- [59] Buck, R. and Giuliano, S. "Solar tower system temperature range optimization for reduced LCOE". In: *SOLARPACES 2018: International Conference on Concentrating Solar Power and Chemical Energy Systems*. AIP Conference Proceedings. AIP Publishing, 2019, page 030010. DOI: 10.1063/1.5117522.
- [60] Winter, C. and Sizmann, R. *Solar Power Plants*. Springer Berlin Heidelberg, 1991.

- [61] Hinkley, J. and Hayward, J. *Cost assessment of hydrogen production from PV and electrolysis*. Report. 2016.
- [62] Brinsmead, T., Hayward, J., and Graham, P. *Australian electricity market analysis report to 2020 and 2030*. Report. 2014.
- [63] Robert Pitz-Paal, Jurgen Dersch, Barbara Milow, Felix Tellez, Alain Ferriere, Ulrich Langnickel, Aldo Steinfeld, Jacob Karni, Eduardo Zarza, and Oleg Popel. "Development Steps for Concentrating Solar Power Technologies With Maximum Impact on Cost Reduction: Results of the European ECOSTAR Study". In: (2005).
- [64] review, W. population. <https://worldpopulationreview.com/country-rankings/median-income-by-country>. 2021.
- [65] Guerra Niehoff, A., Bayer Botero, N., Acharya, A., Thomey, D., Roeb, M., Sattler, C., and Pitz-Paal, R. "Process modelling and heat management of the solar hybrid sulfur cycle". In: *International Journal of Hydrogen Energy* 40.13 (2015), pages 4461–4473. ISSN: 03603199. DOI: 10.1016/j.ijhydene.2015.01.168.
- [66] Bruce, S. *National Hydrogen Roadmap - Pathways to an economically sustainable hydrogen industry in Australia*. Report. 2018.
- [67] Mathias, P. M. and Brown, L. C. *Thermodynamics of the Sulfur-Iodine Cycle for Thermochemical Hydrogen Production*. 2003.
- [68] Mannheim, A. "Assembly and initial operation of a particle heated lab reactor for the decomposition of sulphuric acid". Master's thesis. RWTH Aachen University, 2020.
- [69] Kojo, I. V. and Storch, H. "Copper Production with Outokumpu Flash Smelting: An Update". In: *Sohn International Symposium ADVANCED PROCESSING OF METALS AND MATERIALS* (2006).
- [70] Johnson, W. L., Hauser, D. M., Plachta, D. W., Wang, X.-Y., Banker, B. F., Desai, P. S., Stephens, J. R., and Swanger, A. M. "Comparison of oxygen liquefaction methods for use on the Martian surface". In: *Cryogenics* 90 (2018), pages 60–69. ISSN: 00112275. DOI: 10.1016/j.cryogenics.2017.12.008.
- [71] Halstead, W. D. and Laxton, J. W. "Equilibria in the $\text{Fe}_2(\text{SO}_4)_3/\text{Fe}_2\text{O}_3/\text{SO}_3$ System". In: (1974). DOI: 10.1039/f19747000807.

- [72] Gorenssek, M. B., Meekins, B., Colón-Mercado, H., and Weidner, J. "Parametric study of operating conditions of an SO₂-depolarized electrolyzer". In: *International Journal of Hydrogen Energy* 45.43 (2020), pages 22408–22418. ISSN: 03603199. DOI: 10.1016/j.ijhydene.2020.06.067.
- [73] Moradi, R. and Groth, K. M. "Hydrogen storage and delivery: Review of the state of the art technologies and risk and reliability analysis". In: *International Journal of Hydrogen Energy* 44.23 (2019), pages 12254–12269. ISSN: 03603199. DOI: 10.1016/j.ijhydene.2019.03.041.
- [74] Thomey, D., Lennartz, F., Schöllgen, D., Oliveira, L. de, Säck, J.-P., Roeb, M., and Sattler, C. "DEVELOPMENT AND TEST OF A SOLAR DECOMPOSER OF SULPHURIC ACID FOR THERMOCHEMICAL HYDROGEN PRODUCTION". In: (2011).
- [75] The Linde Group. *Cryogenic Standard Tanks*. Product information sheet. 2021.
- [76] Sattler, C., Roeb, M., Agrafiotis, C., and Thomey, D. "Solar hydrogen production via sulphur based thermochemical water-splitting". In: *Solar Energy* 156 (2017), pages 30–47. ISSN: 0038092X. DOI: 10.1016/j.solener.2017.05.060.
- [77] Que, H., Song, Y., and Chen, C.-C. "Thermodynamic Modeling of the Sulfuric Acid–Water–Sulfur Trioxide System with the Symmetric Electrolyte NRTL Model". In: *Journal of Chemical & Engineering Data* 56.4 (2011), pages 963–977. ISSN: 0021-9568. DOI: 10.1021/je100930y.
- [78] Pitz-Paal, R. "Concentrating Solar Power". In: *Future Energy*. Elsevier, 2020, pages 413–430. ISBN: 9780081028865. DOI: 10.1016/B978-0-08-102886-5.00019-0.
- [79] Petkovic, L. M., Ginosar, D. M., Rollins, H. W., Burch, K. C., Pinhero, P. J., and Farrell, H. H. "Pt/TiO₂ (rutile) catalysts for sulfuric acid decomposition in sulfur-based thermochemical water-splitting cycles". In: *Applied Catalysis A: General* 338.1-2 (2008), pages 27–36. ISSN: 0926860X. DOI: 10.1016/j.apcata.2007.12.016.
- [80] Parma, E., Vernon, M., Gelbard, F., Moore, R., Stone, H., and Pickard, P. *Modeling the Sulfuric Acid Decomposition Section for Hydrogen Production*. Report. 2007.
- [81] Brecher, L. E., Spewock, S., and Warde, C. J. "THE WESTINGHOUSE SULFUR CYCLE FOR THE THERMOCHEMICAL DECOMPOSITION OF WATER". In: *International Journal of Hydrogen Energy* 2 (1977), pages 7–15.

- [82] BHP Group, editor. *Olympic Dam Expansion Draft Environmental Impact Statement 2009*. 2009.
- [83] Barthelemy, H., Weber, M., and Barbier, F. "Hydrogen storage: Recent improvements and industrial perspectives". In: *International Journal of Hydrogen Energy* 42.11 (2017), pages 7254–7262. ISSN: 03603199. DOI: 10.1016/j.ijhydene.2016.03.178.
- [84] Ginosar, D. M., Petkovic, L. M., and Burch, K. C. *Activity and Stability of Sulfuric Acid Decomposition Catalysts for Thermochemical Water Splitting Cycles*. Report. 2005.
- [85] Gelbard, F., Moore, R., Parma, E., Vernon, M., and Stone, H. *Sulfuric Acid Decomposition Experiments for Thermochemical Hydrogen Production from Nuclear Power*. Report. 2007.
- [86] Dodds, P. E., Staffell, I., Hawkes, A. D., Li, F., Grünewald, P., McDowall, W., and Ekins, P. "Hydrogen and fuel cell technologies for heating: A review". In: *International Journal of Hydrogen Energy* 40.5 (2015), pages 2065–2083. ISSN: 03603199. DOI: 10.1016/j.ijhydene.2014.11.059.
- [87] Benitez, D., Buck, R., Dersch, J., and Dibowski, H.-G. *Solarthermische Kraftwerke Wärme, Strom und Brennstoffe aus konzentrierter Sonnenenergie*. Edited by Deutsches Zentrum für Luft- und Raumfahrt e. V. Köln, 2021.
- [88] Corgnale, C., Shimpalee, S., Gorenssek, M. B., Satjaritanun, P., Weidner, J. W., and Summers, W. A. "Numerical modeling of a bayonet heat exchanger-based reactor for sulfuric acid decomposition in thermochemical hydrogen production processes". In: *International Journal of Hydrogen Energy* 42.32 (2017), pages 20463–20472. ISSN: 03603199. DOI: 10.1016/j.ijhydene.2017.06.216.
- [89] Corgnale, C. *High temperature reactor catalyst material development for low cost and efficient solar driven sulfur-based processes*. Report. 2019.
- [90] BROWN, L. C., Besenbruch, G. E., Lentsch, R. D., Schultz, K. R., Funk, J. F., PICKARD, P. S., Marshall, A. C., and Showalter, S. K. "HIGH EFFICIENCY GENERATION OF HYDROGEN FUELS USING NUCLEAR POWER". In: (2003). DOI: 10.2172/814014.

List of Figures

2.1	The HyS process	4
2.2	Bayonet reactor	6
2.3	Heat transfer through a simple pipe	8
2.4	Heliostat on PSA in front and back view, courtesy of DLR/Ernsing [35]	14
2.5	CentRec particle receiver design from Frantz [37]	16
2.6	CentRec measurements optimised by Frantz for the 20 MW receiver [37]	18
3.1	Bayonet reactor measurements	21
3.2	Bayonet reactor model	22
3.3	Oleum reaction model considered by Kaur [46]	24
3.4	Reaction kinetic tests with experimental data from Giaconia [34] for kinetic parameters by Ishikawa [28], van der Merwe [31], Giaconia [34] and Corgnale [47] at 1 bar	25
3.5	(a) Sensitivity check for calculated catalyst bed voidage and (b) Validation of found kinetic parameters with different experimental set-ups by Ginosar [32] and Banerjee [33] for 1 bar	26
3.6	Simplified algorithm flowchart for heat transfer calculations of reaction section in Bayonet model	29
3.7	HyS flowsheet section of sulfuric acid concentration and SAC	35
3.8	Dimensions for BrightSource Energy heliostat [57]	38
3.9	HFLCAL final tower system	39
3.10	Tower system efficiencies at 1st of January 2022	40
3.11	Storage system performance for SM = 4.6, storage size = 19 h, scenario 1a	43
4.1	Parameter study for a) the particle inlet temperature and b) the reaction section inlet temperature	48
4.2	Parameter study for different packing-scenarios	50
4.3	Parameter study for sulfuric acid mass flow rate	51

4.4	Pinch analysis for the complete HyS-cycle	53
4.5	Plant capacity and LCoH over storage size for scenario 3b	56
4.6	CAPEX composition of scenario 1b	58
4.7	Composition of LCoH	59
4.8	Tornado diagrams of sensitivity analysis, green highlighted: conventionally produced hydrogen, blue highlighted: hydrogen produced by standard electrolysis (plant capacity = 85 %)	61
A.1	Plant capacity and LCoH over storage size for scenario 1a	83
A.2	Plant capacity and LCoH over storage size for scenario 1b	84
A.3	Plant capacity and LCoH over storage size for scenario 2	84
A.4	Plant capacity and LCoH over storage size for scenario 3a	85
A.5	Aspen Plus flowsheet of HyS-cycle with integrated Bayonet reactor	85

A Appendix

Techno-economic analysis

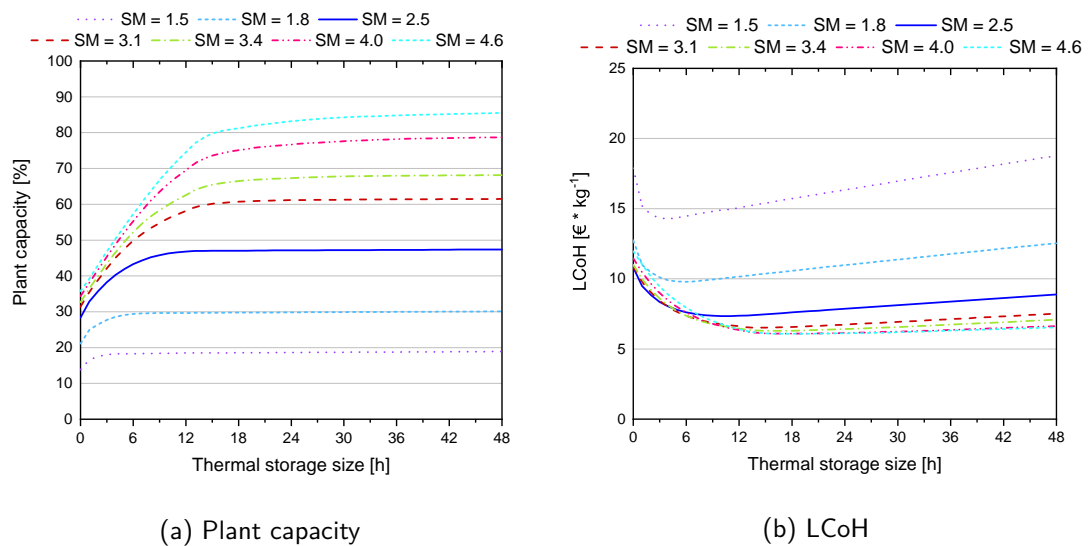
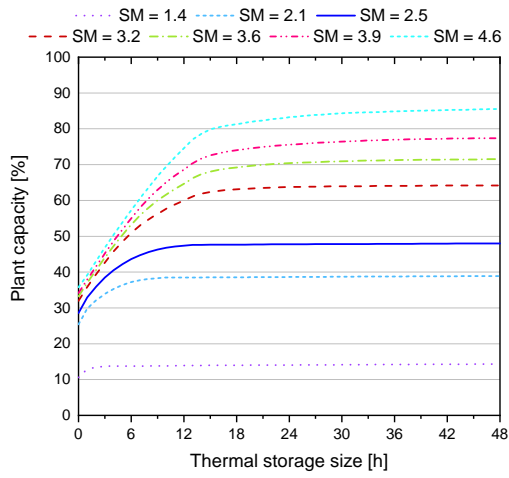
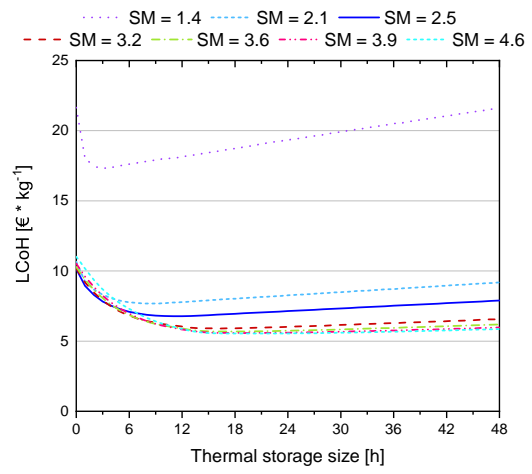


Figure A.1: Plant capacity and LCoH over storage size for scenario 1a

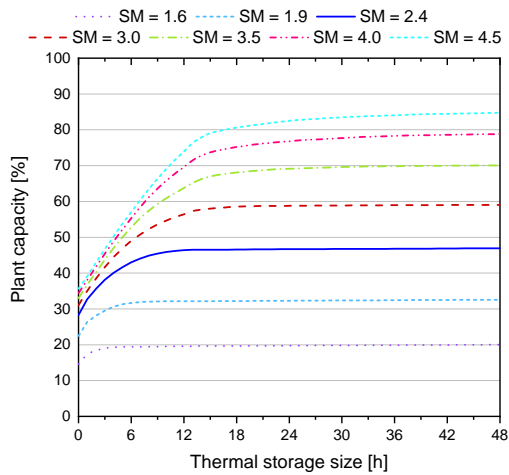


(a) Plant capacity

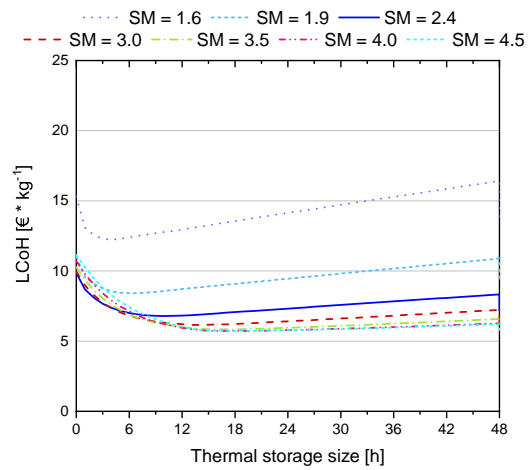


(b) LCoH

Figure A.2: Plant capacity and LCoH over storage size for scenario 1b

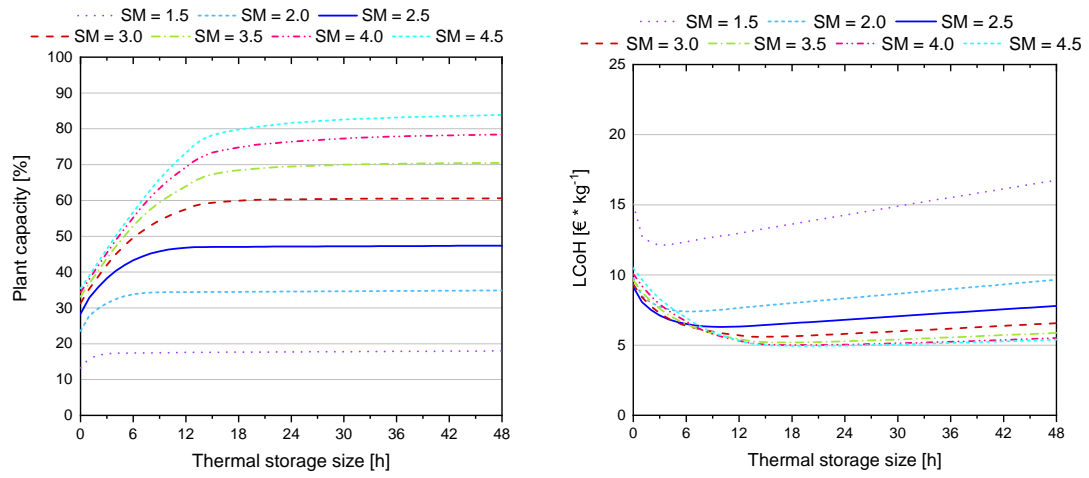


(a) Plant capacity



(b) LCoH

Figure A.3: Plant capacity and LCoH over storage size for scenario 2



(a) Plant capacity

(b) LCoH

Figure A.4: Plant capacity and LCoH over storage size for scenario 3a

Hybrid Sulfur flowsheet

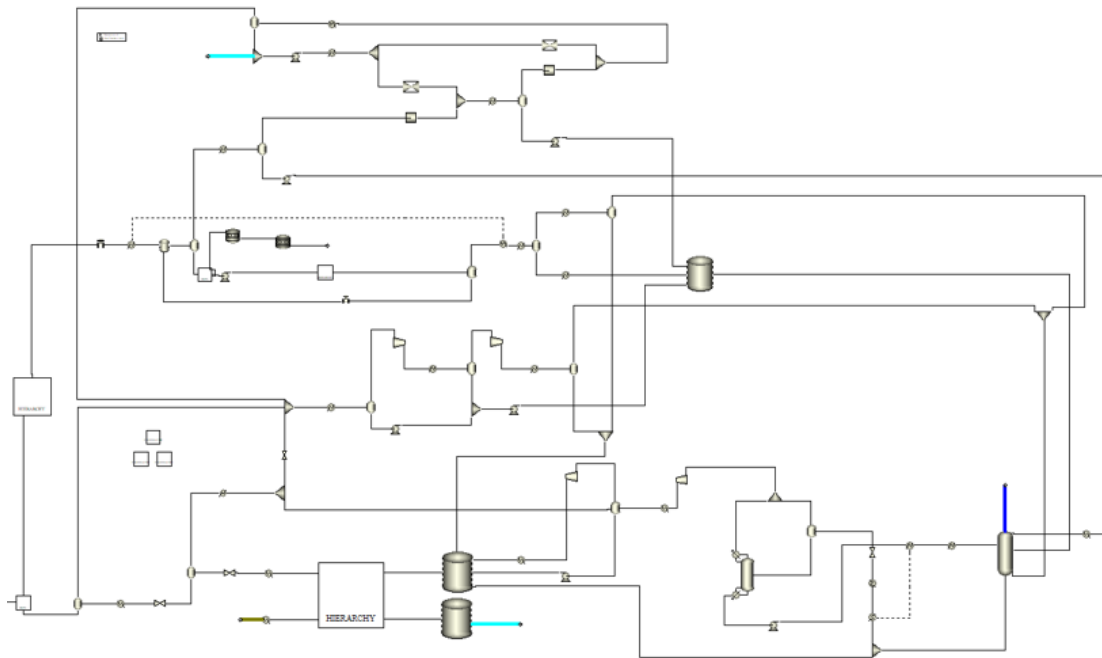


Figure A.5: Aspen Plus flowsheet of HyS-cycle with integrated Bayonet reactor